atoms

MDPI

Review

A Study of the Atomic Processes of Highly Charged Ions Embedded in Dense Plasma

Alok Kumar Singh Jha [1], Mayank Dimri [2,*], Dishu Dawra [2,3] and Man Mohan [2]

1 School of Physical Sciences, Jawaharlal Nehru University, New Delhi 110067, India; alokksjha@mail.jnu.ac.in
2 Department of Physics and Astrophysics, University of Delhi, Delhi 110007, India; dishudawra@ramjas.du.ac.in (D.D.); drmanmohan.05@gmail.com (M.M.)
3 Ramjas College, University of Delhi, Delhi 110007, India
* Correspondence: mdimri79@gmail.com

Abstract: The study of atomic spectroscopy and collision processes in a dense plasma environment has gained a considerable interest in the past few years due to its several applications in various branches of physics. The multiconfiguration Dirac-Fock (MCDF) method and relativistic configuration interaction (RCI) technique incorporating the uniform electron gas model (UEGM) and analytical plasma screening (APS) potentials have been employed for characterizing the interactions among the charged particles in plasma. The bound and continuum state wavefunctions are determined using the aforementioned potentials within a relativistic Dirac-Coulomb atomic structure framework. The present approach is applied for the calculation of electronic structures, radiative properties, electron impact excitation cross sections and photoionization cross sections of many electron systems confined in a plasma environment. The present study not only extends our knowledge of the plasma-screening effect but also opens the door for the modelling and diagnostics of astrophysical and laboratory plasmas.

Keywords: transition energies; radiative decay rates; photoionization; electron impact excitation; dense plasma; ion sphere

check for updates

Citation: Jha, A.K.S.; Dimri, M.; Dawra, D.; Mohan, M. A Study of the Atomic Processes of Highly Charged Ions Embedded in Dense Plasma. *Atoms* **2023**, *11*, 158. https://doi.org/10.3390/atoms11120158

Academic Editor: Frank B. Rosmej

Received: 10 October 2023
Revised: 6 December 2023
Accepted: 11 December 2023
Published: 15 December 2023

1. Introduction

The impact of strongly coupled plasma environment on the atomic structure and collision dynamics of atoms or ions has received much attention during the past few years. The motivation in this field appears due to the improvement in high-resolution spectroscopic experiments for plasma-embedded atoms/ions and several applications in laser-produced plasmas, inertial confinement fusion, X-ray lasers, astrophysical systems and plasma spectroscopy [1–6]. When an atom or ion is subjected to a dense plasma environment, the Coulomb interaction between the bound electrons and the nucleus is shielded by the neighbouring ions and fast electrons. The perturbation of atomic wavefunctions by a nearby free or bound electrons and ions leads to discernible shifts in the emitted spectral lines, ionization potential depression and a significant variation in the collision processes [7–9]. These properties play a vital role in the diagnostics of plasma density and temperature in the emitting region.

The energy levels of an atom/ion immersed in a strongly coupled plasma are depressed by the induced screening potential, which is also known as the ionization potential depression (IPD) for the continuum levels. The study of IPD is of crucial importance for astrophysics [10–13], inertial confinement fusion and solid state physics [14,15]. It has a significant effect on the cross sections of the different atomic processes, such as collisional excitation or ionization [16,17]. During the past few years, several efforts have been made to study the IPD or continuum lowering in dense plasmas [18–45]. On the theoretical side, J. C. Pain [22] presented a quantum statistical model based on a multi configuration description of the electronic structure within the framework of Density Functional Theory. This many-body effect substantially changes the ionization balance and the corresponding charge state distribution, which have a strong influence on the radiative properties of the system [23,24]. J. Zeng et al. [25] investigated the screening potential and IPD of Si plasmas under solar-interior conditions over an electron-density range of $5.88 \times 10^{22} - 3.25 \times 10^{24}$ cm^{-3} and the temperature range of 150–500 eV. Further, the IPDs of heavier Fe plasmas were investigated in near-solid density by J. Zeng et al. [26], by making use of the self-consistent temperature-dependent ion sphere model. Moreover, the self-consistent non-analytical model was also used by J. Zheng et al. [21] to investigate the influence of plasma shielding on the IPD and ionization balance of dense carbon plasma under solar and stellar interior conditions. On the experimental side, new experiments related to the IPD have been performed using high-intensity laser beams at SLAC National Accelerator Laboratory [40,41], at ORION in the United Kingdom [42], at LCLS (Linac Coherent Light Source) [43] and NIF (National Ignition Facility) at Lawrence Livermore National Laboratory [44,45], and the experimentally measured X-ray scattering spectra confirm the direct evidence of the IPDs.

The influence of plasma screening on the excitation energies and transition properties of highly charged ions under a strongly coupled plasma background has witnessed an upsurge in interest in the recent past. Bowen et al. [46] have investigated the plasma-screening effects on the atomic structure and radiative properties of He-like ions immersed in a dense plasma environment using the multi configuration Dirac-Fock method by considering a Debye–Hückel potential. The spectral properties of the low-lying singlet states of a helium atom and those of the low-lying doublet states of a lithium atom in laser plasmas have been calculated by Okustu et al. [47] by making use of a quantum chemical configuration interaction method with a Debye shielding potential. Saha et al. [48] have presented the energy eigenvalues of the doubly excited bound states of a He atom and Li^+ ion under weakly coupled plasma using an explicitly correlated Hylleraas-type basis within the framework of the Rayleigh–Ritz variational method. Saha et al. [49] have also studied the effect of a strongly coupled plasma environment for estimating the excitation energies of the autoionizing states of highly stripped astrophysically important ions Al^{11+}, Si^{12+}, P^{13+}, S^{14+} and Cl^{15+} using the ion sphere model. Using the Debye screening model, Sil et al. calculated [50] the doubly excited states of the highly stripped He-like ions. Further, Belkhiri et al. [51] estimated the ground-state energy shifts for the six most ionized aluminium ions using the ion sphere model. Within the relativistic framework, Chen [52] studied the spectral and decay properties of atoms or ions embedded in a plasma in the presence of applied external electric and magnetic fields. Jin et al. [53] studied the plasma effects on the atomic structure for simulating X-ray free-electron-laser-heated solid-density matter. Li et al. [54] studied the exchange energy shifts between the $1s^2 \rightarrow 1s2p$ $(^3P_1,^1P_1)$ lines of He-like Al ion under a dense plasma environment using both the self-consistent field ion sphere model (SCFISM) and the uniform electron gas model (UEGM). Singh et al. [55] studied the plasma-screening effects on the atomic structure of He-like ions embedded in strongly coupled plasma. The ion sphere model has been employed by Saha et al. [56] to investigate the influence of plasma shielding on the low-lying transitions of Be-like ions. Li et al. [57] reported the influence of dense plasmas on the transition energies and oscillator strengths of Be-like ions for Z = 26–36 using both the SCFISM and UEGM potentials. Recently, Dimri et al. [58] studied the influence of strongly coupled plasma on the low-lying transitions of Be-like ions. Apart from the above discussed theoretical studies, some experimental efforts [59–65] have also been made in the past to study the influence of dense plasma on the spectroscopic properties of atoms/ions. With the development of high-energy, high-intensity optical lasers and X-ray free-electron lasers, it has become feasible to create matter in plasma form [66–68] to perform experimental studies.

Apart from the importance of the fundamental theory, the study of atomic collision processes under extreme conditions plays a crucial role in many areas of physics, such as astrophysics and plasma physics [69–83]. The photoionization process is one of the main atomic processes in the plasma due to its high sensitivity to the detailed atomic structure of many electron systems. Additionally, photoionization exerts a significant effect on the equilibrium state of plasmas. The photoionization cross sections are important for determining the reliable radiative opacity of the dense plasma [84]. Significant theoretical endeavours have been made in the past to study the influence of dense plasma on the photoionization cross sections. Qi et al. [85] investigated the photoionization of hydrogen-like ions in n<=3 bound states, embedded in cold, dense quantum plasmas. Chen et al. [86] studied the photoionization of H-like C ion in the presence of a strongly coupled plasma environment using the ion sphere potential. The photoionization processes of excited hydrogen atom in plasma environments are investigated by Lin et al. [87], using the method of complex coordinate rotation. Further, Rosmej et al. [88] studied the photoionization cross section for complex atoms and ions using the statistical models combined with the local plasma frequency approach. Furthermore, photoionization cross sections for H-like Mg^{11+} and Ni^{27+} ions in finite-temperature dense plasmas have been studied by Ma et al. [89]. Moreover, the effect of a strongly coupled plasma environment on the photoionization cross sections of the H-like O^{7+} ion has been studied by Dawra et al. [90] within the framework of the relativistic configuration interaction technique. The analytical b-potential of Li et al. [91] and the uniform electron gas model potential of Saha et al. [56] have been employed for incorporating the plasma-shielding effects to study the effect on photoionization cross sections.

The influence of plasma on the electron impact excitation of ions is of particular interest as this study provides important information regarding the collision dynamics and physical properties of the neighbouring environment, and has been an active area of research. Deb et al. [92] presented a generalized method for the calculation of inelastic collision strengths for the scattering of electrons by ions in a dense plasma taking account of the shielding of the Coulomb potential by the Debye–Hückel model. The plasma-screening effects on the electron impact excitation of hydrogenic ions in dense plasmas have been studied by Whitten et al. [93], using the Debye–Hückel and ion sphere plasma screening models. Jung et al. [94] investigated the strongly coupled plasma-screening effect on the electron impact excitation of hydrogenic ions. The screening effects on the dipole and quadrupole electron impact excitation of hydrogenic ions in dense high-temperature plasmas were investigated by Kim et al. [76] using the effective pseudopotential model that takes into account both quantum-mechanical and plasma-screening effects. Recently, Chen et al. [95] proposed a novel distorted wave approach within the fundamental framework of relativity theory to calculate the dynamics of magnetic sublevel excitations of the highly charged H-like Ar XVIII ion via an electron impact within a quantum plasma. Very recently, Singh et al. [96] employed the relativistic configuration interaction technique to study the electron impact excitation collision strengths of the H-like Si^{13+} ion in a strongly coupled plasma environment. Moreover, there are also other investigations taking place in a dense plasma environment [97–100].

Considerable investigations have been carried out in the past to study the influence of screening effects in classical hot and dense plasmas [101]. These extensive studies have been motivated mainly in the area of extreme ultraviolet (EUV) and X-ray laser developments, laser-produced plasmas, inertial confinement fusion and astrophysics. The densities (n_e) and temperatures (T) in these plasmas span the ranges n_e~10^{19}–10^{21} cm^{-3}, T~50–300 eV for laser-produced plasmas and n_e~10^{22}–10^{26} cm^{-3}, T~0.5–10 keV for inertial confinement fusion plasmas [102]. Both Coulomb and thermal effects play vital roles in classical hot and dense plasmas. The relative importance of Coulomb and thermal effects can be evaluated by the plasma coupling parameter $\Gamma = \frac{\langle Z_i e \rangle^2}{R_i K_B T_e}$, where $\langle Z_i e \rangle$ denotes the average charge of ions in the plasma, $R_i = \left(\frac{3}{4\pi n_e}\right)^{1/3}$ is the average inter ionic distance, T_e and n_e are the plasma electron temperature and density, respectively, and k_B is the Boltzmann constant. For the weakly coupled plasmas ($\Gamma << 1$) with low densities and high temperatures, the

Coulomb energy is comparatively small compared to the thermal energy, and self-consistent long-range interactions dominate over two-particle short-range interactions.

The generalized form of the screened Coulomb potential (V_{sc}) is given by [103–108]

$$V_{sc}(r) = -Ze^2\left(\frac{1}{r} - \frac{1}{D + D_A}\right), r < D_A$$

and

$$V_{sc}(r) = -Ze^2\frac{D}{D + D_A}\frac{1}{r}exp\left(-\left(\frac{r - D_A}{D}\right)\right), r \geq D_A \tag{1}$$

where Z is the nuclear charge, D_A and $D = \frac{(K_B T_c)^{\frac{1}{2}}}{(4\pi e^2 n_e)^{\frac{1}{2}}}$ are the mean minimum radius of the ion sphere and the screening length, respectively. In the limit when $D_A \to 0$, Equation (1) reduces to Debye–Hückel (Yukawa-type) potential [109,110] and is defined as

$$V_{sc}(r) = \frac{-Ze^2}{r}exp\left(-\frac{r}{D}\right) \tag{2}$$

On the other hand, for strongly coupled plasmas ($\Gamma >> 1$) with high density and low temperature, the potential energy dominates over the kinetic energy. Here, the ions are closely packed with each other and each ion is surrounded by a sphere of radius $R_i = \left(\frac{3}{4\pi n_e}\right)^{1/3}$, known as the ion sphere radius. In the strongly coupled plasma, the screened potential of the plasma-embedded atomic system is given by [111–113]

$$V_{sc}(r) = \frac{-Ze^2}{r}\left[1 - \frac{r}{2R_i}\left(3 - \frac{r^2}{R_i^2}\right)\right] \text{ for } \mathrm{R} \leq \mathrm{R_i}$$

and

$$V_{sc}(r) = 0 \text{ for } r \geq R_i \tag{3}$$

Recently, the effect of plasma screening on the atomic structure properties has also been modelled by the analytical b-potential of Li and Rosmej [114] given by

$$V_{sc} = \frac{-Z}{r} + \frac{N_f}{R_0}\left[1 + \frac{1}{x-1} - \frac{1}{x-1}\left(\frac{r}{R_0}\right)^{x-1}\right], \tag{4}$$

$$\text{with } R_0 = \left[3N_f/4\pi n_e\right]^{1/3}; N_f = Z - N_b \text{ and } x = 3 - \frac{b}{\pi}\sqrt{\frac{N_f}{R_0 T_e}}$$

where R_0, n_e, r, N_b and N_f represent the radius of the ion sphere, electron density, radial coordinate of the electron, number of bound electrons and the number of free electrons inside the ion sphere, respectively. T_e stands for the temperature of electron and b is a parameter that characterizes the self-consistent electron distribution inside the ion sphere. The multiconfiguration Dirac-Fock self-consistent finite temperature ion sphere model (MCDF-SCFTIS) simulations are matched with b ≈ 2 for Maxwellian electron distribution. When x = 3 (T_e is infinite), Equation (4) corresponds to the UEGM potential [2] which can be given as

$$V_{sc}(r, R_0) = \frac{-Z}{r} + \frac{N_f}{2R_0}\left[3 - \left(\frac{r}{R_0}\right)^2\right]. \tag{5}$$

We have incorporated these screened Coulomb potentials in our calculations and then studied the effect of the plasma environment on the excitation energies, radiative decay rates, oscillator strengths, photoionization cross sections and electron impact excitation cross sections for highly charged ions.

This review summarizes the impact of perturbing plasmas on the electronic structures, transition properties, and collision dynamics of atoms/ions under a dense plasma environment. It is in the above context that we have modified the Dirac-Coulomb Hamiltonian by incorporating the uniform electron gas model (UEGM) and analytical plasma screening (APS) potentials in the multiconfiguration Dirac-Fock method (MCDF) and the relativistic configuration interaction theory (RCI). In our models, the modified Dirac equations are solved numerically to obtain the bound and continuum state wavefunctions. The investigation of atomic structure and collision dynamics for H-, He- and Be-like ions has been carried out since these systems are abundant in plasma and their emission lines are beneficial for plasma diagnostics. Further, for large densities, there appears a level crossing that is important for experimental identification [115].

This review is structured as follows. In Section 2, we have briefly discussed the theoretical methods used for the calculation of atomic structure calculations, photoionization cross sections, and electron impact excitation cross section calculations. Section 3 is devoted to the results of our findings and a brief summary is provided in Section 4.

2. Methods of Calculation

2.1. Plasma-Embedded Atomic Structure Calculations

In the presence of external environments, structural and spectroscopic properties of atomic systems (neutral atoms and ions) become modified. In the ion sphere model, the ion is enclosed in a spherically symmetric cell that contains the exact number of electrons to ensure the neutrality condition.

The UEGM potential:

The influence of plasma shielding on the various atomic structure properties is modelled by the UEGM potential [2] and given as

$$V_{IS}(r,R_0) = \frac{-Z}{r} + \frac{Z-N_b}{2R_0}\left[3-\left(\frac{r}{R_0}\right)^2\right], \tag{6}$$

$$\text{with } R_0 = \left[3N_f/4\pi n_e\right]^{1/3};\ N_f = Z - N_b \tag{7}$$

Here, r is the radial coordinate of the electron, N_b signifies the number of bound electrons, N_f is the number of free electrons inside the ion sphere, R_0 is the ion sphere radius and the electron density is given by n_e.

The analytical plasma screening (APS) potential:

The other potential to model the influence of plasma shielding is the analytical plasma screening (APS) potential, the so-called "b-potential" of Li et al. [114], given by

$$V^{APS} = \frac{-Z}{r} + \frac{N_f}{R_0}\left[1 + \frac{1}{\left(3-\frac{b}{\pi}\sqrt{\frac{N_f}{R_0T_e}}\right)-1} - \frac{1}{\left(3-\frac{b}{\pi}\sqrt{\frac{N_f}{R_0T_e}}\right)-1}\left(\frac{r}{R_0}\right)^{(3-\frac{b}{\pi}\sqrt{\frac{N_f}{R_0T_e}})-1}\right] \tag{8}$$

where T_e is the electron temperature and parameter b is nearly 2 for the Maxwell-Boltzmann distribution.

The UEGM and APS potential have been included in the MCDF and RCI methods. Further, the radial components of the wavefunction satisfy the normalization condition

$$\int_0^\infty \left[P_{nk}{}^2(r) + Q_{nk}{}^2(r)\right] dr = 1 \tag{9}$$

For higher values of free electron density, the bound electron wave functions might not be equal to 0 outside the ion sphere.

2.1.1. The Multi-Configuration Dirac-Fock (MCDF) Method

To execute the extensive calculations, the MCDF (fully relativistic) method [116] was employed. The Breit and QED corrections have also been taken into consideration.

The atomic state functions (ASFs) for N-electron system are linear combinations of n-electronic configuration state functions (CSFs)

$$|\psi_\alpha\ (PJM)\rangle = \sum_{i=1}^{n} C_i(\alpha)|\gamma_i\ (PJM)\rangle \tag{10}$$

where CSFs $\gamma_i(PJM)$ are linear combinations of Slater determinants with well-defined parity and angular momentum PJM. The expansion mixing coefficients $C_i(\alpha)$ for each configuration state function (CSF) satisfy the followingrelation

$$(C_i(\alpha))^\dagger C_j(\alpha) = \delta_{ij} \tag{11}$$

with ASFs satisfying the orthonormality condition and αdenotes denoting the coupling orbital occupation numbers. Diagonalizing the Dirac-Coulomb Hamiltonian yields the mixing coefficients for N-electron atom/ion

$$\hat{H}^{DC} = \sum_{i=1}^{N} \hat{H}_i + \sum_{i=1}^{N-1} \sum_{j=i+1}^{N} \frac{1}{\left|\hat{r}_i - \hat{r}_j\right|} \tag{12}$$

where $\hat{H}_i$ is the one-electron Hamiltonian given by

$$\hat{H}_i = c\vec{\alpha}_i.\vec{p}_i + \beta mc^2 + V_{nuc} \tag{13}$$

where in Equation (13), the first two terms signify electron kinetic energy whereas the last term gives the Coulomb potential of the nucleus, c represents the speed of light and α and β are 4×4 Dirac matrices.

The one-electron Dirac spinor ϕ_{nkm} is given as follows

$$\phi_{nkm} = \frac{1}{r}\begin{pmatrix} P_{nk}(r) & \chi_{km}(\theta,\phi,\sigma) \\ -iQ_{nk}(r) & \chi_{-km}(\theta,\phi,\sigma) \end{pmatrix} \tag{14}$$

where $P_{nk}(r)$ and $Q_{nk}(r)$ are the large and small components of one-electron radial functions, n is the principal quantum number, k denotes the Dirac angular quantum number, whereas m is the projection of total angular momentum. $\chi_{km}(\theta,\phi)$ is the spin orbit function given by

$$\chi_{km}(\theta,\phi) = \sum_{\sigma=\pm\frac{1}{2}} \left\langle lm - \sigma\frac{1}{2}\sigma \middle| l\frac{1}{2}jm \right\rangle Y_l^{m-\sigma}(\theta,\phi)\phi^\sigma \tag{15}$$

Here, $Y_l^{m-\sigma}(\theta,\phi)$ is a spherical harmonic function, σ represents the electron spin z-projection quantum number and θ is polar angle whereas ϕ is azimuthal angle.

2.1.2. Relativistic Configuration Interaction (RCI) Calculations

RCI utilizes a fully relativistic configuration interaction approach [117] which is applied to ions with high nuclear charge and is based on the Dirac equation. This method has also been successfully used in our previous works [118–124]. RCI calculates the various atomic radiative and collisional processes, including energy levels, radiative transition rates, ionization and collisional excitation by electron impact, photoionization, autoionization, dielectronic capture and radiative recombination. The collisional radiative model is included to construct synthetic spectra of plasmas under various physical conditions.

The energy levels of N-electrons' atom/ion are acquired by diagonalizing the relativistic Hamiltonian H

$$H = \sum_{i=1}^{N} H_D(i) + \sum_{i<j}^{N} \frac{1}{r_{ij}} \tag{16}$$

where $H_D(i)$, represents the single-electron Dirac Hamiltonian given by

$$\hat{H}_D(i) = c\alpha.p + (\beta - 1)c^2 + V_{nuc} \tag{17}$$

The atomic state functions are given as

$$\Psi = \sum_v b_v \phi_v \tag{18}$$

where the mixing coefficients b_v are obtained by diagonalizing H with respect to the basis ϕ_v.

2.2. Methods Incorporating the Plasma-Shielding Effect

2.2.1. MCDF in a Dense Plasma Environment

To consider the effect of plasma screening on the spectral properties, the Dirac-Coulomb Hamiltonian comprising all the dominant interactions is given as

$$\hat{\mathrm{H}}^{\mathrm{DC}} = \sum_{\mathrm{i}=1}^{\mathrm{N}} \hat{\mathrm{H}}_{\mathrm{i}} + \sum_{\mathrm{i}=1}^{\mathrm{N}-1} \sum_{\mathrm{j}=\mathrm{i}+1}^{\mathrm{N}} \frac{1}{|\hat{\mathrm{r}}_{\mathrm{i}} - \hat{\mathrm{r}}_{\mathrm{j}}|} \tag{19}$$

where the one-electron Hamiltonian $\hat{H}_i$ is expressed by

$$\hat{\mathrm{H}}_{\mathrm{i}} = \mathrm{c}\vec{\alpha}_{\mathrm{i}}.\vec{\mathrm{p}}_{\mathrm{i}} + \beta \mathrm{mc}^2 + V_{IS}(r,\ R_0). \tag{20}$$

Here, the first two terms signify the relativistic kinetic energy of a bound electron and the last term $V_{IS}(r, R_0)$ represents the modified potential experienced by the bound electron within the ion sphere.

2.2.2. The RCI Method Incorporating the Plasma-Shielding Effect

In this approach, the Hamiltonian for N-electron atom or ion immersed in a dense plasma environment has the following form

$$\hat{H} = \sum_{i=1}^{N} \hat{H}_D(i) + \sum_{i<j}^{N} \frac{1}{r_{ij}}, \tag{21}$$

where the single-electron Dirac-Hamiltonian $\hat{H}_D(i)$ is given as

$$\hat{H}_D(i) = c\alpha.p + (\beta - 1)c^2 + V_{IS}(r, R_0) \tag{22}$$

2.3. The Continuum Wavefunction Incorporating the Plasma-Screening Effect

The theoretical model employed for the evaluation of continuum wavefunctions is based on the distorted wave approximation. The continuum wavefunction [117] is determined by solving the following differential equations

$$\left(\frac{d}{dr} + \frac{k}{r}\right) P_{nk}(r) = \alpha\left(\varepsilon_{nk} - V^N(r) - V^{ee}(r) - V_{IS} + \frac{2}{\alpha^2}\right) Q_{nk}(r)$$

$$\left(\frac{d}{dr} - \frac{k}{r}\right) Q_{nk}(r) = \alpha(-\varepsilon_{nk} + V^N(r) + V^{ee}(r) + V_{IS}) P_{nk}(r) \tag{23}$$

where α is the fine structure constant and ε_{nk} depicts the energy eigenvalues of the radial orbitals. $V^N(r)$ and $V^{ee}(r)$ denote the attractive nuclear potential and the repulsive electron–electron interaction potential, respectively.

2.4. Photoionization and Radiative Recombination Cross Section Calculations

Under the dipole approximation, the photoionization cross sections are evaluated using the above wavefunctions [117]. The relativistic photoionization cross section is given by

$$\sigma_{PI} = 2\pi\alpha \frac{1 + \alpha^2\varepsilon}{1 + 0.5\alpha^2\varepsilon} \frac{df}{dE} \tag{24}$$

and the radiative recombination cross section is given by the Milne relation [117]

$$\sigma_{RR} = \frac{\alpha^2}{2} \frac{g_i}{g_f} \frac{\omega^2}{\varepsilon(1 + 0.5\alpha^2\varepsilon)} \sigma_{PI} \tag{25}$$

where α is the fine structure constant, g_i and g_f are the statistical weights of the initial and final bound states, ω is the photon energy, ε stands for the photoelectron energy, and $\frac{df}{dE}$ denotes the oscillator strength given by

$$\frac{df}{dE} = \frac{\omega}{g_i} [L]^{-1} (\alpha\omega)^{2L-2} S, \tag{26}$$

where L is the rank of the multipole operator, $[L]$ stands for $2L + 1$ and the generalized line strength S is given by

$$S = \sum_{kJ_T} |\langle \Psi_f, k; J_T \| O^L \| \Psi_i \rangle|^2, \tag{27}$$

where k is the relativistic quantum number of free electrons, J_T denotes the total angular momentum of the free state, and O^L is the multiple operator inducing the transition.

2.5. Electron Impact Excitation and Collision Strength Calculations

The collision dynamics of the atomic system are solved using the matrix mechanics within the framework of relativistic distorted wave (RDW) theory. Mathematical and technical details of the RDW approximation have been discussed elsewhere [117].

For transitions occurring from the initial to the final state ($\psi_i \rightarrow \psi_f$), the electron impact excitation cross section is defined as

$$\sigma_{if} = \frac{\pi}{g_i k_i^2} \sum_{K_i} \sum_{K_f} \sum_{J_T} (2J_T + 1) \left| \left\langle \psi_i, K_i, J_T, M_T \middle| \sum_{p<q} \left(\frac{1}{r_{pq}} \right) \middle| \left(\psi_f, K_f, J_T, M_T \right) \right\rangle \right|^2$$

$$\sigma_{if} = \Omega_{if} \frac{\pi}{g_i k_i^2} \tag{28}$$

where Ω_{if} represents the collision strength, g_i is the statistical weight of the initial level of the target ion, k_i denotes the kinetic momentum and energy of the incident electron, J_T is the total angular momentum, and M_T stands for the projection of the total angular momentum.

3. Results and Discussion

In this section, we present the effect of a dense plasma environment on the atomic structure of He- and Be-like ions. First, we discuss the plasma-shielding effect on the structural properties of He-like ions followed by Be-like ions [55,58].

3.1. The Study of He-like Ions in a Dense Plasma Environment

Figure 1 displays the line shifts of the $1s^{2\,1}S_0 \rightarrow 1s3p\,^1P_1^o$ He-β transition of the Cl^{15+} ion immersed in dense plasmas described by kT and n_e in the range of 600–1000 eV and 2×10^{23}—–1×10^{24}cm^{-3}, respectively. It is evident from Figure 1 that for a given kT, the line shifts of the Cl^{15+} ion increase with the increase in electron densities. The present results are compared with the recent high-resolution measurements of Beiersdorfer et al. [59]. The theoretically predicted line shifts from the MCDF method are 1.96 eV (1.92 eV), 3.94 eV (3.86 eV) and 5.92 eV (5.80 eV) for $n_e = 2 \times 10^{23}$, 4×10^{23} and 6×10^{23} cm^{-3}, with kT = 600 eV (650 eV), respectively. A good agreement has been observed between the theoretical line shifts and the experimental measurements. A better agreement can also be seen between our MCDF and RCI line shifts.

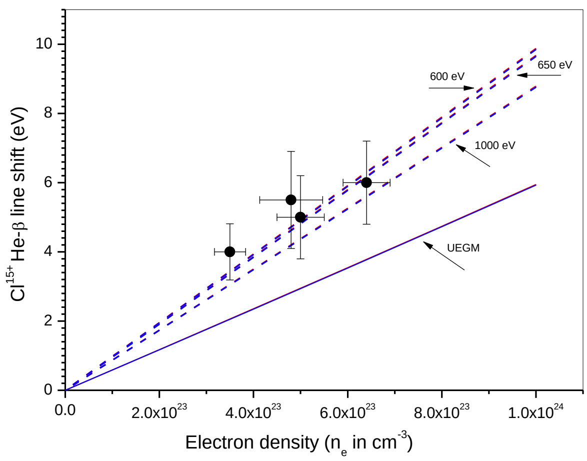

Figure 1. Line shift variation of the $1s^{2\,1}S_0 \rightarrow 1s3p\,^1P_1^o$ He–β transition of Cl^{15+} ion with the electron density for electron temperatures 600–1000 eV. Experimental measurements [59] are shown by dots with an error bar, our APS potential results from RCI and MCDF methods by dashed blue and red lines, and our RCI and MCDF UEGM results by solid blue and red lines (adapted from [55]).

The relative variation in the electron binding energies with the electron density for Ar^{16+}, Ti^{20+} and Fe^{24+} ions at kT = 600 eV is depicted in Figure 2 using the MCDF and RCI methods. The relative variation in binding energy (BE) is defined as

$$\text{Relative variation in } BE = \frac{[\,BE(n_e \neq 0) - BE(n_e = \ 0)] \times 100}{BE(n_e = \ 0)} \quad (29)$$

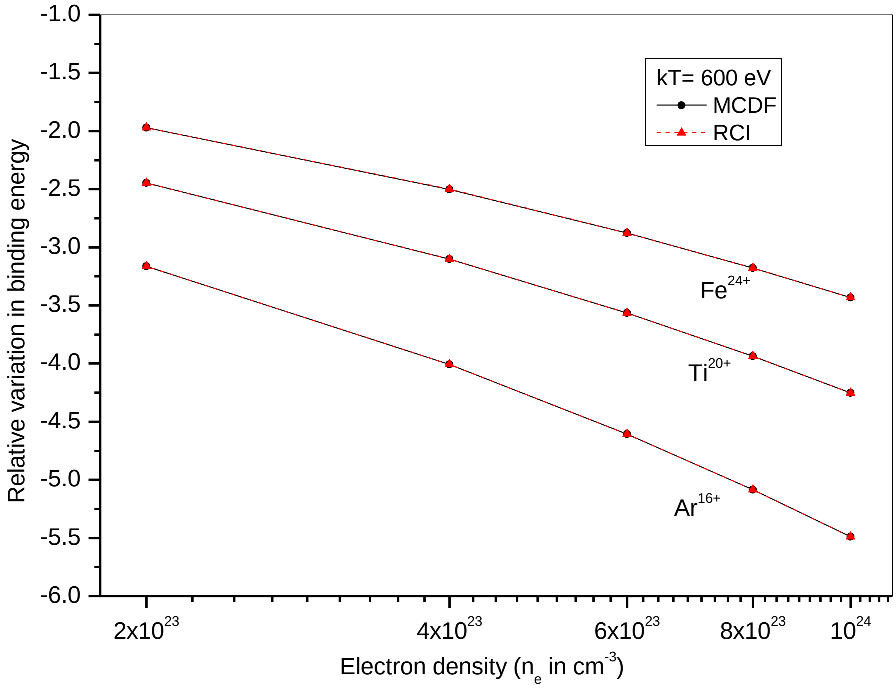

Figure 2. Relative variation in binding energies for Ar^{16+}, Ti^{20+} and Fe^{24+} ions as a function of free electron density by APS potential (adapted from [55]).

An inspection of Figure 2 shows that binding energies decrease monotonically with the increase in electron densities. This behaviour is due to the screening of the Coulomb potential via the free electrons. Moreover, the drop in binding energy decreases with increasing nuclear charge, i.e., the binding energy of the Ar^{16+} ion decreases more quickly compared to Ti^{20+} and Fe^{24+} ions with increasing densities. Also, a satisfactory agreement has been found between the MCDF and RCI methods. Our theoretical results for the unperturbed ions match well with the experimental [125] values.

Figures 3–5 show the graphical variation of our plasma energy shifts for both the intercombination and resonance transitions of Ar^{16+}, $Ti^{20+}$and Fe^{24+} ions at various values of kT and n_e. It is interesting to observe that the shifts of the excitation energiesincrease with an increase in free electron densities for a given kT. For the $1s^2\ ^1S_0 \rightarrow 1s3p\ ^1P_1^o$ transition of the Ar^{16+} ion, our MCDF (RCI) plasma shifts are about 1.78 eV (1.78 eV) and 9.04 eV (9.01 eV) for electron densities 2×10^{23} and 1×10^{24} cm^{-3} at kT = 600 eV, respectively. A good agreement can be seen between our presented MCDF and RCI plasma energy shifts. Further, with the increase in kT, the plasma energy shift decreases. It is a consequence of the fact that with increasing kT, the shielding effect becomes weakened between the nucleus and electrons, since more and more electrons are distributed farther away from the nucleus. For instance, when $n_e = 1 \times 10^{24}$ cm^{-3}, the MCDF plasma energy shifts for the $1s^2\ ^1S_0 \rightarrow 1s3p\ ^1P_1^o$ transition of the Ar^{16+} ion are around 9.04 and 7.97 eV at kT = 600 and 1000 eV, respectively. Such shifts can be estimated in dense plasma spectroscopic experiments, assuming that the observed emission lines are adequately narrow, and Stark shifts and self-absorption do not deform the line profiles beyond recognition. It can be seen from Figures that the plasma energy shifts calculated using the UEGM potential increase with an increase in electron densities.

Furthermore, with an increasing nuclear charge, the shift of the transition energies decreases. The influence of plasma screening becomes relatively less important for a given kT and n_e for a higher nuclear charge in view of the fact that the binding energy of the bound electrons increases with the increase in nuclear charge. For the $1s^2\ ^1S_0 \rightarrow 1s3p\ ^3P_1^o$ transition, the MCDF plasma energy shift is about 8.88 eV for the Ar^{16+} ion and 5.28 eV for the Fe^{24+} ion at kT = 600 eV and $n_e = 1 \times 10^{24}$ cm^{-3}.

It is interesting to note that the plasma energy shift is less pronounced for the $(1s2p\ ^3P_1^o)$ lower-lying state as this state is strongly bound by the nuclear attraction and remains relatively less affected at low densities.

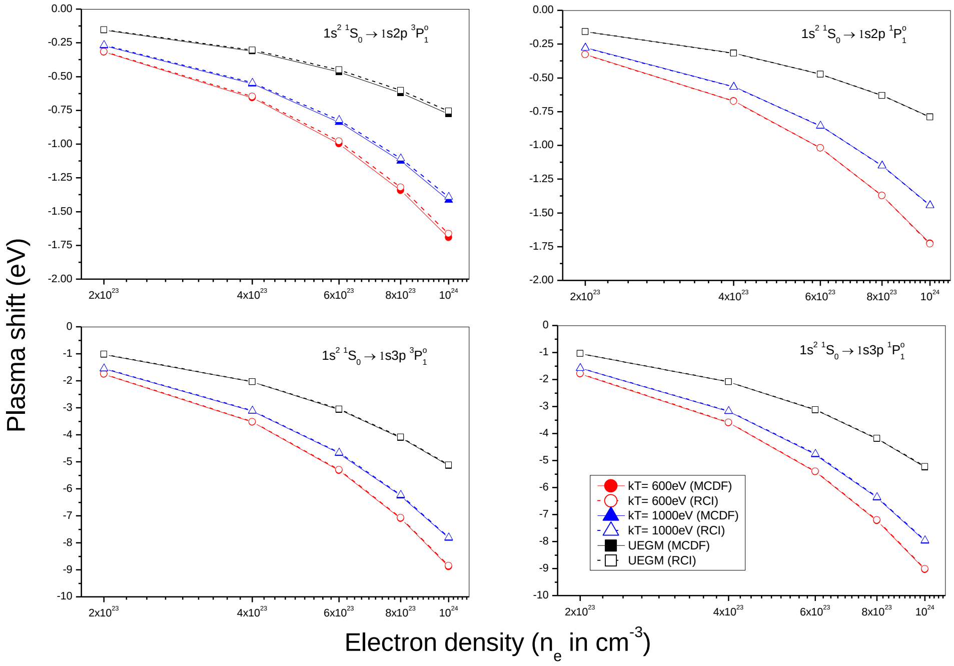

Figure 3. Plasma energy shift for the inter-combination $1s^{2\,1}S_0 \rightarrow 1snp^3P_1^o$ (n = 2, 3) and resonance $1s^{2\,1}S_0 \rightarrow 1snp\ ^1P_1^o$ (n = 2, 3) transitions of He-like Ar^{16+} ion with respect to free electron density. The blue and red curves are APS, while black is UEGM, which is temperature-independent (adapted from [55]).

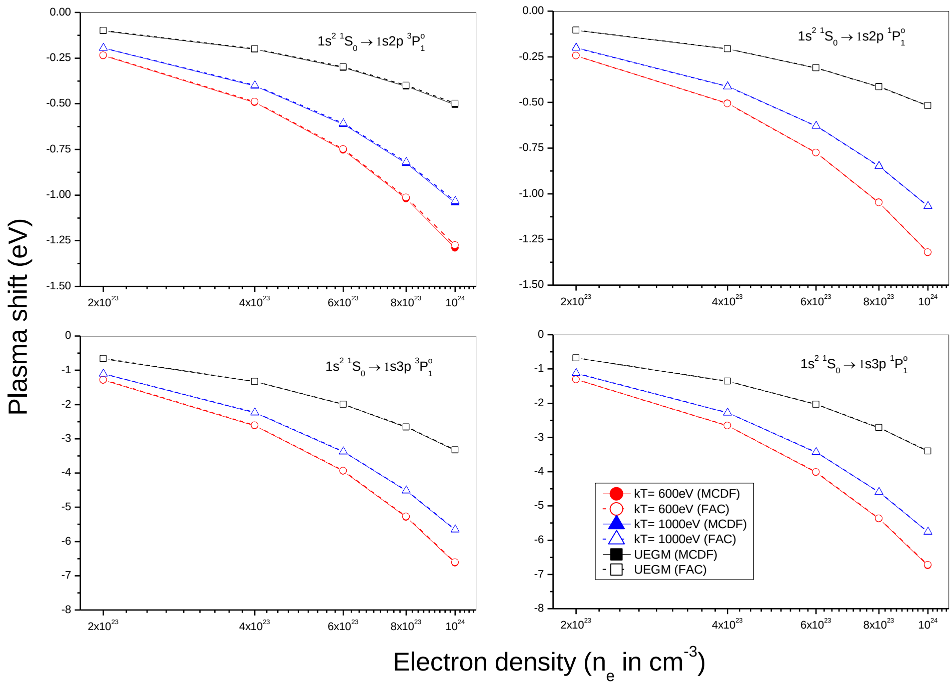

Figure 4. Plasma energy shift for the inter-combination $1s^{2\,1}S_0 \rightarrow 1snp^3P_1^o$ (n = 2, 3) and resonance $1s^{2\,1}S_0 \rightarrow 1snp^1P_1^o$ (n = 2, 3) transitions of He-like Ti^{20+} ion with respect to free electron density. The blue and red curves are APS, while black is UEGM, which is temperature-independent (adapted from [55]).

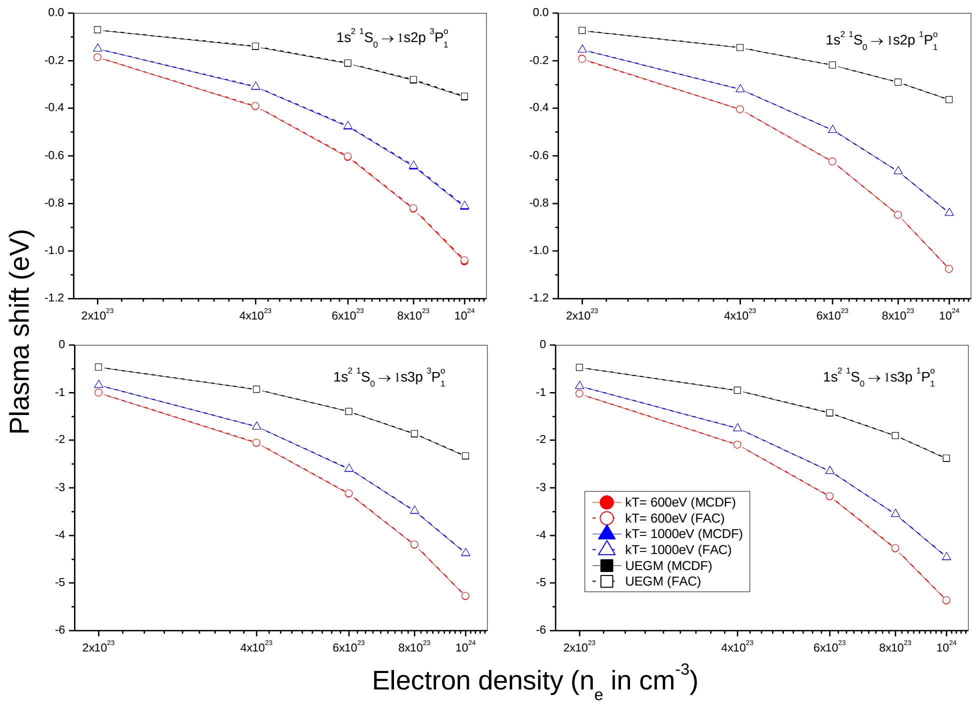

Figure 5. Plasma energy shift for the inter-combination $1s^{2\,1}S_0 \rightarrow 1snp^3P_1^o$ (n = 2, 3) and resonance $1s^{2\,1}S_0 \rightarrow 1snp^1P_1^o$ (n = 2, 3) transitions of He-like Fe^{24+} ion with respect to free electron density. The blue and red curves are APS, while black is UEGM, which is temperature-independent (adapted from [55]).

Figure 6 illustrates the ratio (R) of the radiative decay rates of the resonance $1s^{2\,1}S_0 \rightarrow 1s3p\ ^1P_1^o$ to inter-combination $1s^2\ ^1S_0 \rightarrow 1s3p\ ^3P_1^o$ transition of the Ar^{16+} ion with respect to free electron density at kT = 600 eV from the MCDF method. This ratio plays a pivotal role in deriving the electron density and plasma temperature in the emitting region. A larger plasma energy shift has been seen for the ($1s^{2\,1}S_0 \rightarrow 1s3p\ ^1P_1^o$) resonance line when compared to the inter-combination line, thereby increasing the ratio with an increase in plasma density. For instance, the effect of plasma screening on this ratio is about 0.20% and 1.15% for $n_e = 2 \times 10^{23}$ and 1×10^{24} cm^{-3}, respectively, which is too small for experimental detection at present.

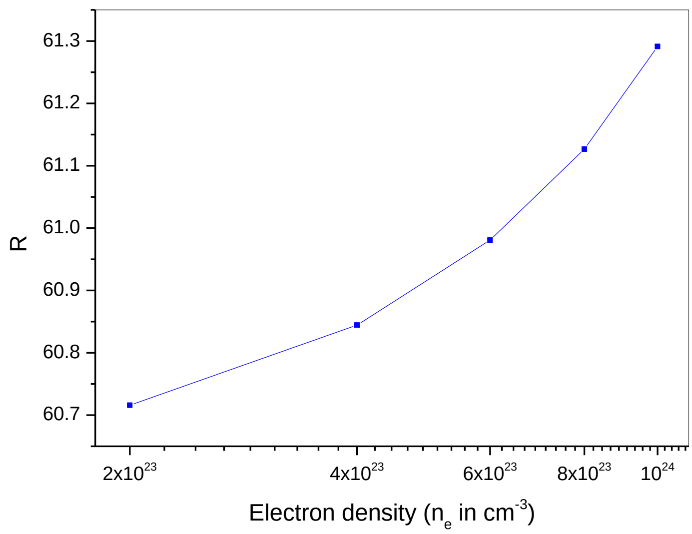

Figure 6. Ratio R of the radiative decay rates of the resonance-to-inter-combination transitions of Ar^{16+} ion as a function of the free electron density at kT = 600 eV using the APS potential (adapted from [55]).

3.2. The Study of Be-like Ions in a Dense Plasma Environment

In Figure 7 the variation of plasma energy shifts for inter-combination and resonance transitions of Be-like ions has been displayed with respect to free electron density using the MCDF and RCI methods. It is clear from the figure that the shift of the transition energies increases with increasing plasma densities, whereas it decreases with increasing nuclear charge. Since the binding energy of the bound electrons increases with the increase in nuclear charge, the influence of plasma screening becomes less pronounced for a given n_e for higher nuclear charge. For the $2s^2$ ($^1S_0$) $\rightarrow$ 2s3p ($^3P_1^o$) transition, the MCDF plasma energy shift for electron densities 1.0×10^{22} and 5.0×10^{23} cm^{-3} is about 0.0898 and 4.7375 eV for the Si^{10+} ion, whereas it is around 0.0217 eV and 1.0558 eV for the Fe^{22+} ion. A good agreement can be seen between our plasma energy shifts from both theoretical methods. Moreover, we see that the shift is less pronounced for the 2s2p $^3P_1^o$ state as this state is strongly bound by the nuclear attraction and remains comparatively less influenced at smaller plasma densities.

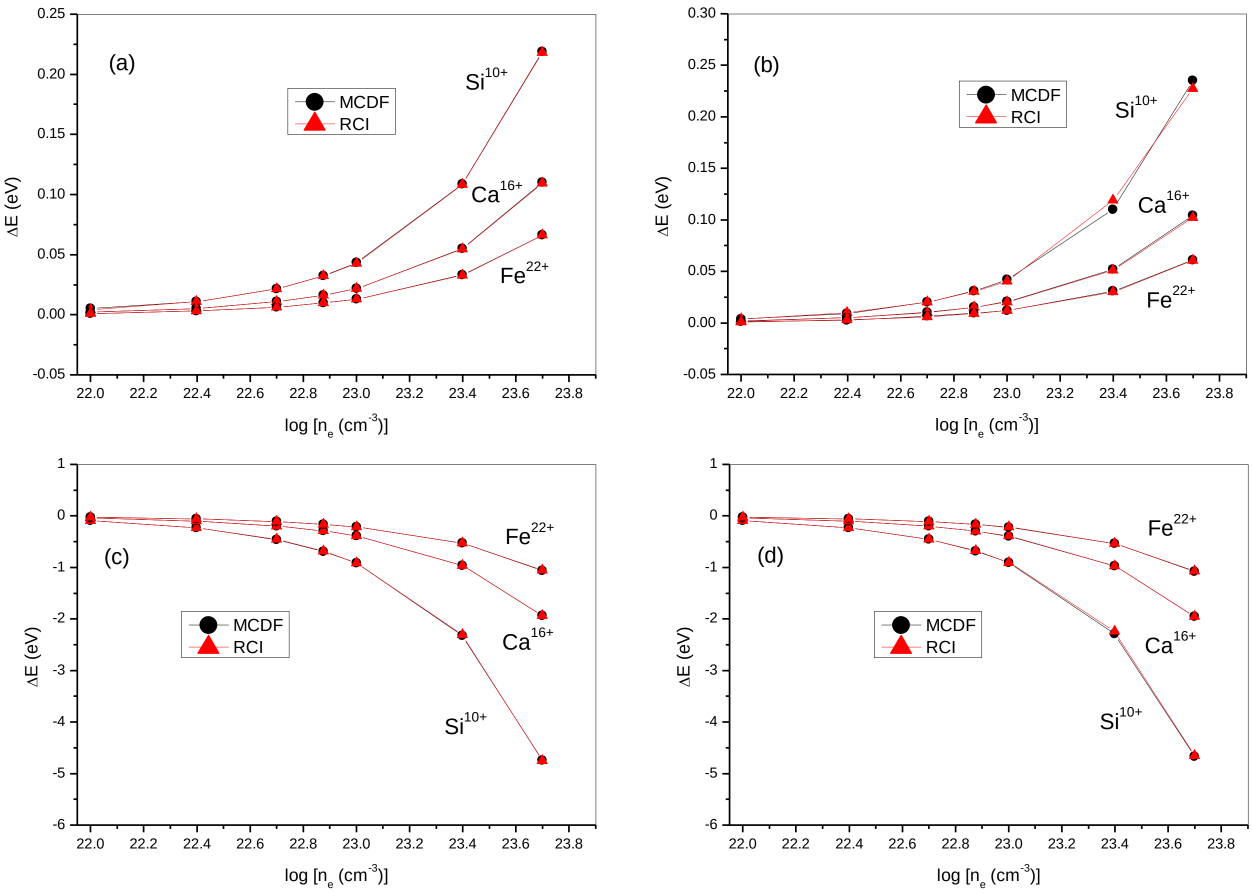

Figure 7. Plasma energy shift (ΔE) for the inter-combination and resonance transitions as a function of the free electron density for Si^{10+}, Ca^{16+} and Fe^{22+} ions. Panels (**a**,**b**) correspond to $2s^2\,^1S_0 \rightarrow$ 2s2p ($^3P_1^o$, $^1P_1^o$) transitions, whereas (**c**,**d**) correspond to $2s^2\,^1S_0 \rightarrow$ 2s3p ($^3P_1^o$, $^1P_1^o$) transitions, respectively (adapted from [58]).

The pressure experienced by an atom or ion inside the ion sphere of radius R can be evaluated from the first law of thermodynamics. Under an adiabatic approximation, the pressure on the ion in the ground state can be written as

$$P = -\frac{1}{4\pi R^2}\frac{dE}{dR} \tag{30}$$

where 'E' is the ground state energy of the concerned ion. In Table 1 we have provided the calculated pressure P for the ground state of compressed Be-like Si^{10+}, Ca^{16+} and Fe^{22+} ions at different ion sphere radii R. The nature of the variation in pressure with the ion sphere radius remains the same for Be-like Si^{10+}, Ca^{16+} and Fe^{22+} ions. It is evident from Table 1 that at low values of ion sphere radius, the generated pressure tends to become very high, which pushes the system toward instability.

Table 1. Thermodynamic pressure on the ground state of Be-like Si^{10+}, Ca^{16+} and Fe^{22+} ions within the ion sphere (adapted from [58]).

n_e (cm^{-3})	R (au)	Pressure Si^{10+} (Pa)		R (au)	Pressure Ca^{16+} (Pa)		R (au)	Pressure Fe^{22+} (Pa)	
		MCDF	RCI		MCDF	RCI		MCDF	RCI
1.0×10^{22}	11.73	7.426×10^{9}	7.426×10^{9}	13.72	6.350×10^{9}	6.350×10^{9}	15.25	5.711×10^{9}	5.711×10^{9}
2.5×10^{22}	8.64	2.519×10^{10}	2.519×10^{10}	10.11	2.154×10^{10}	2.154×10^{10}	11.24	1.938×10^{10}	1.938×10^{10}
5.0×10^{22}	6.86	6.345×10^{10}	6.345×10^{10}	8.02	5.428×10^{10}	5.428×10^{10}	8.92	4.882×10^{10}	4.882×10^{10}
7.5×10^{22}	5.99	1.089×10^{11}	1.089×10^{11}	7.01	9.320×10^{10}	9.320×10^{10}	7.79	8.383×10^{10}	8.383×10^{10}
1.0×10^{23}	5.44	1.598×10^{11}	1.598×10^{11}	6.37	1.368×10^{11}	1.368×10^{11}	7.08	1.230×10^{11}	1.230×10^{11}
2.5×10^{23}	4.01	5.414×10^{11}	5.414×10^{11}	4.69	4.638×10^{11}	4.638×10^{11}	5.22	4.173×10^{11}	4.173×10^{11}
5.0×10^{23}	3.18	1.362×10^{12}	1.362×10^{12}	3.72	1.168×10^{12}	1.168×10^{12}	4.14	1.051×10^{12}	1.051×10^{12}

3.3. Photoionization in a Dense Plasma Environment

In the photoionization process, one deals with the (e^-+ion) system with an electron in the continuum. The photoionization process for the ground state of O VIII is given as

$$\text{O VIII } (1s^2S_{1/2}) + h\nu \rightarrow \text{O IX} + e^-$$

In our RCI calculations [90], we used an atomic model containing six configurations 1s, 2s, 2p, 3s, 3p and 3d owing to the fact that there was an absence of electron correlation effects in H-like ions. The photoionization of the ground state $1s\,^2S_{1/2}$ or an excited state $nl\,^2L_J$ of H-like ions leaves a bare ion with a monotonically weakening interaction with respect to the ejected photoelectron energy. The ionization potential depression (IPD) is defined as the difference of the ionization potential of the unperturbed ion (UI) and screened ion (SI), i.e., $\Delta E = E(\text{UI}) - E(\text{SI})$. The variation in the ionization potential depression of the H-like O^{7+} ion in the ground state as a function of free electron density at kT = 200, 600 and 1000 eV, respectively, has been illustrated in Figure 8. It can be easily seen from Figure 8 that the ionization potential depression significantly increased with increasing n_e when the ion was subjected to a dense plasma environment. For instance, the ionization potential depression was about 2.77 and 78.95 eV for electron densities 1.0×10^{19} and 2.0×10^{23} cm^{-3} at kT = 200 eV. Also, there was a decrease in ionization potential depression with an increasing value of kT for a given n_e.

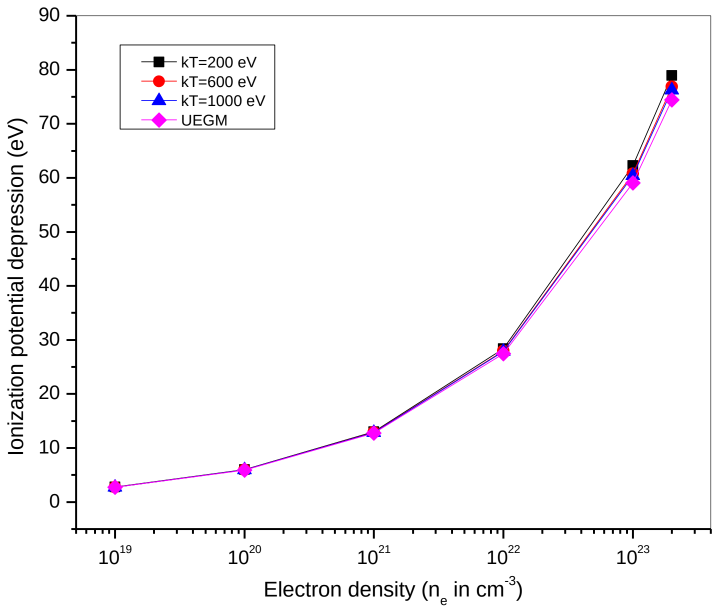

Figure 8. Ionization potential depression of the 1s state of H-like O^{7+} as a function of the free electron density (adapted from [90]).

Within the framework of the Kramers approach [126], a simple analytical expression for the photoionization cross section of an atomic subshell with quantum numbers nl can be written as

$$\sigma_{nl}^{Kr}(\omega) = \frac{64\pi}{3\sqrt{3}} N_{nl} \frac{a_0^2}{cZ^2} \sqrt{\frac{Ry}{I_{nl}}} \left(\frac{I_{nl}}{\hbar\omega}\right)^3 \quad (31)$$

where Z is the nuclear charge, I_{nl} is the ionization potential of the nl state and ω is the ionizing radiation frequency. The above expression corresponds to the photoionization cross section for the ground state of hydrogen atom assuming that Z = N_{nl} = 1 and I_{nl} = Ry (Ry = 13.6 eV). Therefore, a comparison of the photoionization cross sections for the $1s_{1/2}$ state of the isolated H-like O^{7+} ion as a function of photon energy with the cross sections evaluated from the Kramers approach has been made in Figure 9. At the ionization threshold, the exact known value for the photoionization cross section for the ground state of hydrogen atom is 6.3 Mb. The cross section comes out to be 0.098.

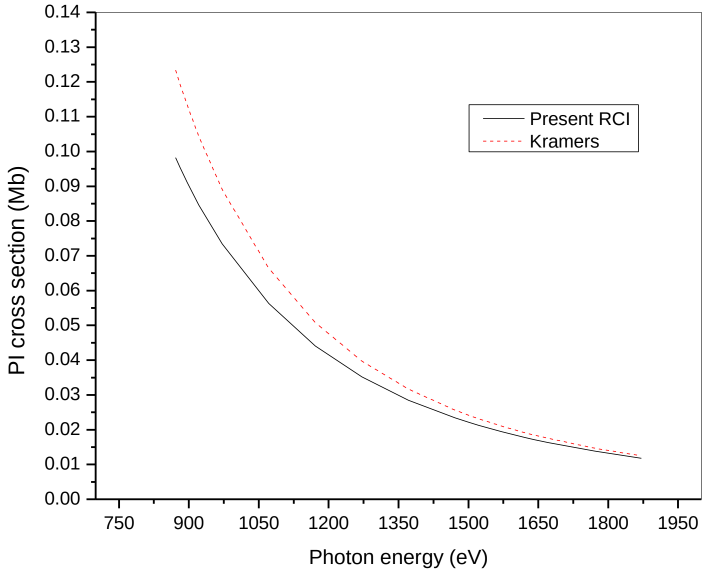

Figure 9. The photoionization cross sections for the ground state of isolated H-like O^{7+} ion as a function of the photon energy (adapted from [90]).

Mb if Z-scaling is used for H-like O^{7+} ion. The photoionization cross sections calculated from the RCI and the Kramers approach at the ionization threshold are 0.098 and 0.123 Mb. It is worth mentioning that an excellent agreement is obtained between our RCI cross section and the exact value of the cross section for the H-like O^{7+} ion.

The photoionization cross sections for the $1s_{1/2}$, $2s_{1/2}$, $2p_{3/2}$ and $3p_{1/2}$ states of the H-like O^{7+} ion subjected to dense plasmas with respect to the photon energy have been depicted in Figure 10a–d using the APS and UEGM potentials. For the above mentioned states, the photoionization cross sections have been studied at different values of n_e and kT. The photoionization cross section of hydrogenic systems generally decreases monotonically with respect to photon energy.

However, near the ionization threshold, the photoionization cross sections of H-like O^{7+} show very different behaviours. The photoionization cross section has a maximum, then a minimum, and then strongly increases when going from high to low photon energies. With increasing photon energy, a minimum known as the Cooper minimum arises when the electron density is adequately high enough. This is due to the reason that the sufficient plasma screening changes the core potential and the normal hydrogenic behaviour is expected to break down near the ionization threshold. The usual monotonically decreasing behaviour of the photoionization cross section is observed in the region of higher photon energy.

With the increase in electron densities, one can easily observe that the ionization thresholds move to the low energy region. The photoionization cross section values increase with increasing n_e at a fixed value of kT as the decreased ionization threshold changes the continuum wave function of the photoelectron, hence the dipole transition matrix element is changed correspondingly. Furthermore, the photoionization cross sections decrease with the increase in kT for a fixed value of electron density. For the photoionization of the $1s_{1/2}$ state of the O^{7+} ion, our evaluation shows that at kT = 200 eV and the photoionization cross sections at the ionization threshold increase by about 64% and 317%, respectively, at 1.0×10^{19} and 1.0×10^{23} cm^{-3}, in comparison to the isolated ion cross sections. Further, the plasma-shielding effect is less pronounced for lower-lying states than compared to higher-lying states.

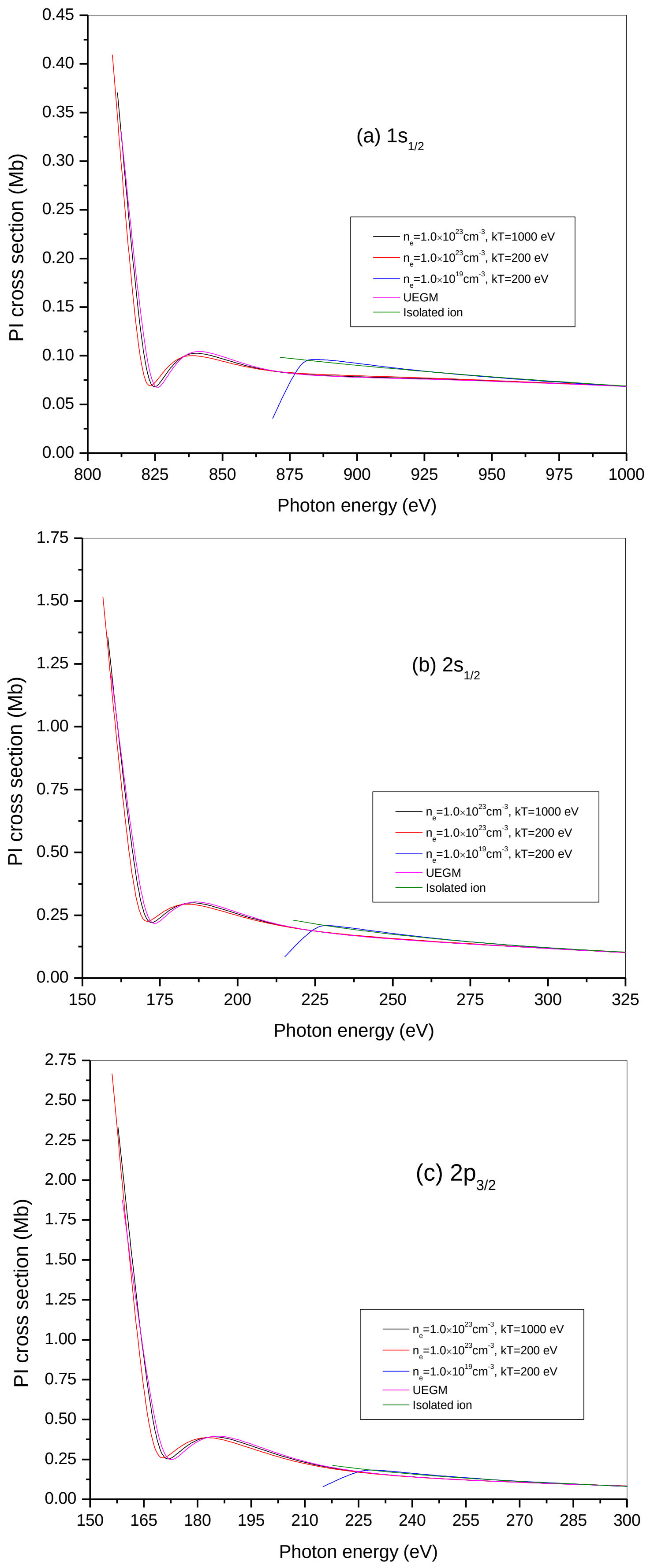

Figure 10. *Cont*.

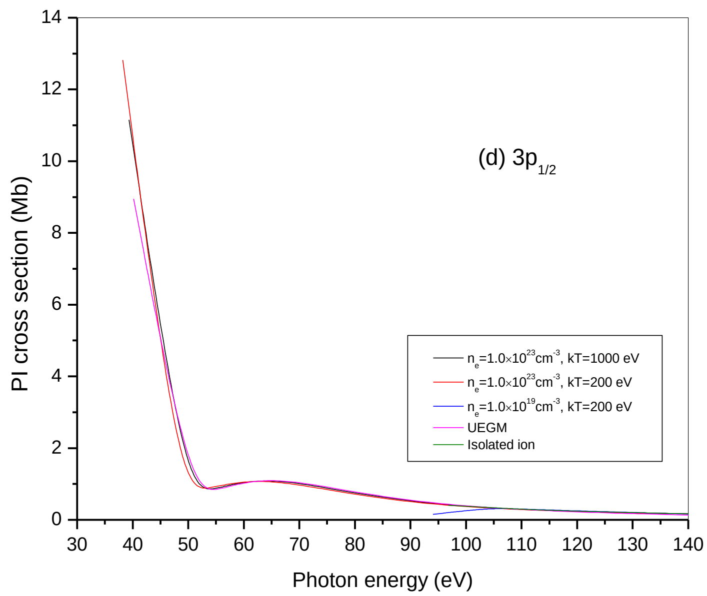

Figure 10. (**a**) Variation of the photoionization cross sections of $1s_{1/2}$ state with respect to photon energy from the present RCI calculations with APS and UEGM potentials for different values of plasma screening (adapted from [90]). (**b**) Variation of the photoionization cross sections of $2s_{1/2}$ state with respect to photon energy from the present RCI calculations with APS and UEGM potentials for different values of plasma screening (adapted from [90]). (**c**) Variation of the photoionization cross sections of $2p_{3/2}$ state with respect to photon energy from the present RCI calculations with APS and UEGM potentials for different values of plasma screening (adapted from [90]). (**d**) Variation of the photoionization cross sections of $3p_{1/2}$ state with respect to photon energy from the present RCI calculations with APS and UEGM potentials for different values of plasma screening (adapted from [90]).

3.4. Electron Impact Excitation in a Dense Plasma Environment

The electron impact excitation processes in a dense plasma environment are of particular interest since the line emission, due to excitation, provides important information regarding the physical properties of the surrounding environments. Conventionally, the selection of a configuration set including all important electron correlations is crucial for the construction of good target wave functions to achieve reliable and accurate results. Therefore, for the electron impact excitation calculation [96], the same atomic model consisting of the same six configurations has been considered. The variation of the potential $-rV_{IS}(r)$ with respect to the radial distance from the nucleus for (a) the isolated Si XIV ion and (b) the Si XIV ion at kT = 200 eV and n_e = 2.0 × 10^{23}, 1.0 × 10^{24} cm^{-3}, respectively, has been displayed in Figure 11. It is worth noting that the potential declines much faster with r as the electron density increases due to the spreading of more and more free electrons around the nuclear charge. It can be seen from the plot that for both densities, the potential tends to approach the value of one, which is the net charge of the screened nucleus and can be observed at the boundary of the sphere.

For a better demonstration, the variation of collision strength with respect to incident electron energy for the excitation from the $1s_{1/2}$ to the $2p_{1/2}$ state when subjected to plasma for n_e = 2.0 × 10^{23} cm^{-3} and 1.0 × 10^{24} cm^{-3} at kT = 200 eV and 1000 eV is shown in Figure 12. The collision strength calculations for the free case have also been presented. The collision strengths show an increasing pattern with incident electron energy. It can be observed that collision strength decreases with an increase in electron density for a fixed value of kT. This is due to the fact that the presence of the plasma considerably lowers the total cross section for all the incoming projectile (electron) energies under consideration as the long-range coupling matrix element is particularly sensitive to shielding. Furthermore, the increase in kT collision strength exhibits a rise for a fixed value of electron density.

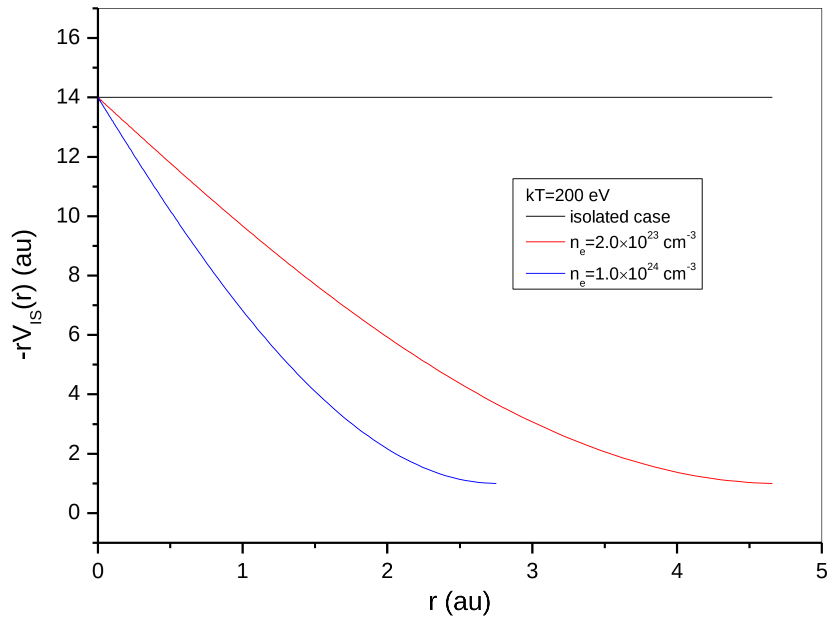

Figure 11. Variation of the potential $-rV_{IS}(r)$ as a function of radial distance from the nucleus for Si XIV at kT = 200 eV and $n_e = 2.0 \times 10^{23}$ and 1.0×10^{24} cm^{-3} (adapted from [96]).

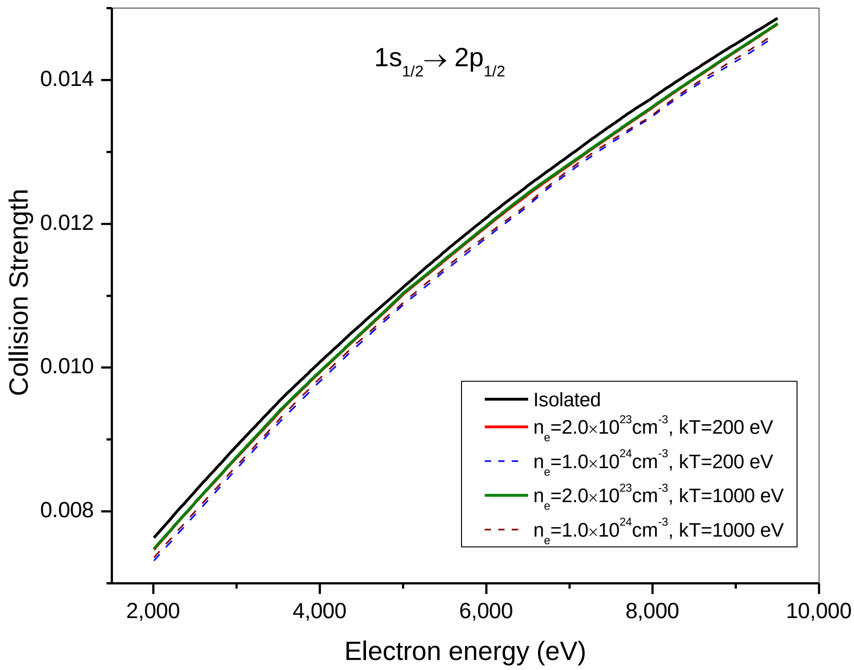

Figure 12. Variation of collision strength with respect to incident electron energy (in eV) for the $1s_{1/2} \rightarrow 2p_{1/2}$ transition for (i) isolated ion, (ii) ion immersed in a plasma at electron density $n_e = 2.0 \times 10^{23}$ cm^{-3} and 1.0×10^{24} cm^{-3} at the temperatures 200 eV and 1000 eV (adapted from [96]).

The collision strength as a function of electron energy (in eV) for the transition from the $2s_{1/2}$ to the $3p_{1/2}$ state for the plasma densities 2.0×10^{23} cm^{-3} and 1.0×10^{24} cm^{-3} at the temperatures 200 eV and 1000 eV has been shown in Figure 13. A close inspection of Figure 13 reveals that the observations from Figure 12 are further reiterated, wherein collision strength decreases with the increase in n_e (at a fixed kT) and increases with the rise in kT (at a fixed n_e). When compared to the free case, the collision strength of the $2s_{1/2} \rightarrow 3p_{1/2}$ transition at incident electron energy 2377 eV when subjected to dense plasma with $n_e = 2.0 \times 10^{23}$ cm^{-3} and 1.0×10^{24} cm^{-3} decreases by 6.45% and 9.88% at kT = 200 eV. Further, for $n_e = 1.0 \times 10^{24}$ cm^{-3}, the collision strength at the incident electron energy of 9500 eV increases by about 4.99% at kT = 1000 eV, when compared to kT = 200 eV.

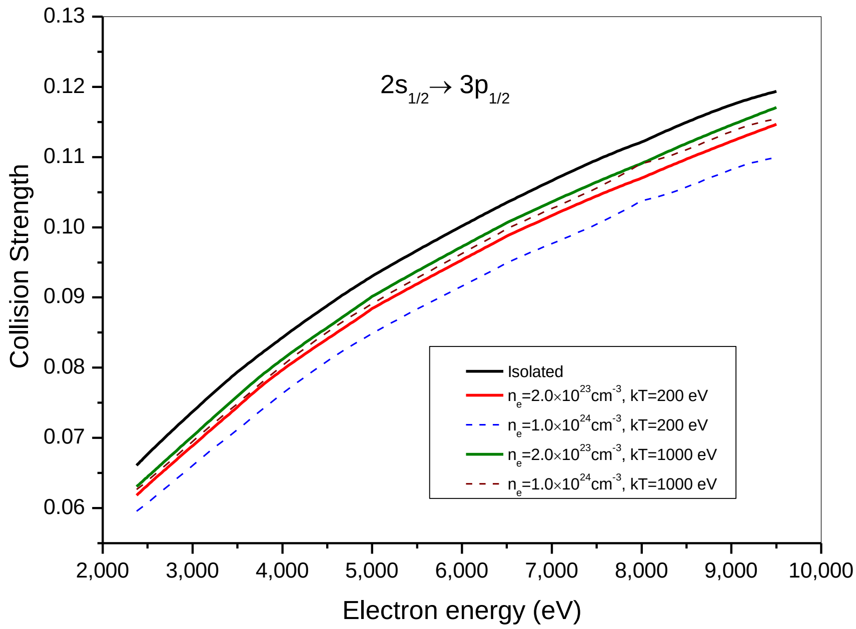

Figure 13. Variation of collision strength with respect to incident electron energy (in eV) for the $2s_{1/2} \rightarrow 3p_{1/2}$ transition for (i) isolated ion, (ii) ion immersed in a plasma at electron density $n_e = 2.0 \times 10^{23}$ cm^{-3} and 1.0×10^{24} cm^{-3} at the temperatures 200 eV and 1000 eV (adapted from [96]).

4. Conclusions

To summarize, the multiconfiguration Dirac-Fock (MCDF) method and the relativistic configuration interaction (RCI) technique incorporating the uniform electron gas model (UEGM) and analytical plasma screening (APS) potentials have been employed for characterizing the interactions among the charged particles in plasma. We have presented the line shifts of the $1s^{2\,1}S_0 \rightarrow 1s3p\ ^1P_1^o$ He-β transition of the Cl^{15+} ion subjected to dense plasma. Our predicted line shifts are in good agreement with the experimental measurements. Further, the effect of plasma screening on the transition energies of the inter-combination $1s^{2\,1}S_0 \rightarrow 1snp\ ^3P_1^o = 2, 3$ and the resonance $1s^2\ ^1S_0 \rightarrow 1snp\ ^1P_1^o = 2, 3$ transitions of the He-like Ar^{16+}, $Ti^{20+}$and Fe^{24+} ions has been analyzed. Also, the influence of plasma shielding has been investigated on the transition energies of the inter-combination $2s^{2\,1}S_0 \rightarrow 2snp\ ^3P_1^o$ (n = 2, 3) and the resonance $2s^{2\,1}S_0 \rightarrow 2snp\ ^1P_1^o$ (n = 2, 3) transitions for the Be-like Si^{10+}, Ca^{16+} and Fe^{22+} ions. Our theoretical results for the isolated case match well with the experimental values. Further, we have investigated the photoionization cross sections of the H-like O^{7+} ion embedded in a dense plasma environment. The calculations for the ionization potentials and photoionization cross sections of O^{7+} ion were carried out in the density and temperature ranges of $n_e = 1.0 \times 10^{19}-2.0 \times 10^{23}$ cm^{-3} and T_e = 200–1000 eV, respectively. A significant ionization potential depression was found with increasing free electron densities. The photoionization cross sections increase with the increase in n_e for a fixed kT, while they decrease with increasing kT for a fixed n_e. Moreover, the effect of a dense plasma environment on the electron impact excitation cross sections of the H-like Si^{13+} ion was investigated using the relativistic configuration interaction technique by incorporating the plasma-screening effects. It is very interesting that the photoionization cross sections increase while the collisional excitation cross sections decrease with the increase in free electron density for a fixed kT. Furthermore, we found an increase in collision strengths with increasing kT for a fixed free electron density. This review summarizes the impact of perturbing plasmas on the electronic structures, transition properties, and collision dynamics of atoms/ions under a dense plasma environment that may be of interest in the high-energy density plasma community. The limitation of the present approach is that it is unable to deal with fluctuations, either static (Plasma Polarisation Shift) or dynamic. Further precise experimental measurements are suggested to support this spectral analysis.

Author Contributions: The contributions of each author to this work are as follows: Conceptualization, A.K.S.J. and M.D.; theoretical investigation, D.D.; visualization, M.M.; validation, A.K.S.J. and M.M.; writing—original draft, A.K.S.J.; writing—review and editing, M.M., D.D. and M.D.; resources, A.K.S.J.; supervision, M.M. All authors have read and agreed to the published version of the manuscript.

Funding: This work has been supported by the DST-SERB (India) under the Grant No. CRG/2022/008061.

Data Availability Statement: The data presented in this study are available on request from the corresponding author.

Acknowledgments: Dishu Dawra and Mayank Dimri are thankful to Deen Dayal Upadhyaya College for their constant motivation and encouragement. Alok K. S. Jha is thankful to Jawaharlal Nehru University for providing the necessary computational resources.

Conflicts of Interest: The authors declare no conflict of interest.

References

1. Murillo, M.S.; Weisheit, J.C.; Hansen, S.B.; Dharma-Wardana, M.W.C. Partial Ionization in Dense Plasmas: Comparisons among Average-Atom Density Functional Models. *Phys. Rev. E* **2013**, *87*, 063113. [CrossRef] [PubMed]
2. Belkhiri, M.; Poirier, M. Density effects in plasmas: Detailed atomic calculations and analytical expressions. *High Energy Density Phys.* **2013**, *9*, 609–617. [CrossRef]
3. Nantel, M.; Ma, G.; Gu, S.; Côté, C.Y.; Itatani, J.; Umstadter, D. Pressure Ionization and Line Merging in Strongly Coupled Plasmas Produced by 100-Fs Laser Pulses. *Phys. Rev. Lett.* **1998**, *80*, 4442–4445. [CrossRef]
4. Chen, Z.B.; Zhao, G.P.; Qi, Y.Y. Theoretical studies of the spectral characteristics and electron impact dynamics of Ti XXI placed in the hot dense regimes. *J. Electron Spectrosc. Relat. Phenom.* **2023**, *262*, 147283. [CrossRef]
5. Renner, O.; Rosmej, F.B. Challenges of X-ray spectroscopy in investigations of matter under extreme conditions. *Matter Radiat. Extrem.* **2019**, *4*, 024201.
6. Rosmej, F.B.; Astapenko, V.A.; Lisitsa, V.S. *Plasma Atomic Physics*; Springer: Heidelberg, Germany, 2021; Volume 650.
7. Chen, Z.B. Study of atomic spectroscopy and electron collision process in non-ideal classical plasmas. *Phys. Plasmas* **2023**, *30*, 052105. [CrossRef]
8. Griem, H.R. *Principles of Plasma Spectroscopy*; Cambridge University Press: Cambridge, UK, 2005.
9. Salzmann, D. *Atomic Physics in Hot Plasmas*; Oxford University Press: New York, NY, USA, 1988.
10. Rogers, F.J.; Iglesias, C.A. Astrophysical Opacity. *Science* **1994**, *263*, 50–55. [CrossRef]
11. Guillot, T. Interiors of giant planets inside and outside the solar system. *Science* **1999**, *286*, 72–77. [CrossRef]
12. Potekhin, A.Y.; Massacrier, G.; Chabrier, G. Equation of state for partially ionized carbon at high temperatures. *Phys. Rev. E* **2005**, *72*, 046402. [CrossRef]
13. Massacrier, G.; Potekhin, A.Y.; Chabrier, G. Equation of state for partially ionized carbon and oxygen mixtures at high temperatures. *Phys. Rev. E* **2011**, *84*, 056406. [CrossRef]
14. Lindl, J.D.; Amendt, P.; Berger, R.L.; Glendinning, S.G.; Glenzer, S.H.; Haan, S.W.; Kauffman, R.L.; Landen, O.L.; Suter, L.J. The physics basis for ignition using indirect-drive targets on the National Ignition Facility. *Phys. Plasmas* **2004**, *11*, 339–491. [CrossRef]
15. Hu, S.X.; Militzer, B.; Goncharov, V.N.; Skupsky, S. Strong Coupling and Degeneracy Effects in Inertial Confinement Fusion Implosions. *Phys. Rev. Lett.* **2010**, *104*, 235003. [CrossRef]
16. Jarrah, W.; Pain, J.C.; Benredjem, D. Plasma potential and opacity calculations. *High Energy Density Phys.* **2019**, *32*, 8–13. [CrossRef]
17. Pain, J.-C.; Benredjem, D. Simple electron-impact excitation cross-sections including plasma density effects. *High Energy Density Phys.* **2021**, *38*, 100923. [CrossRef]
18. Liu, P.; Gao, C.; Hou, Y.; Zeng, J.; Yuan, J. Transient space localization of electrons ejected from continuum atomic processes in hot dense plasma. *Commun. Phys.* **2018**, *1*, 95–101. [CrossRef]
19. Lin, C. Ionization Potential Depression and Ionization Balance in Dense Plasmas. *arXiv* **2019**, arXiv:1904.04456.
20. Lin, C. Quantum statistical approach for ionization potential depression in multi-component dense plasmas. *Phys. Plasmas* **2019**, *26*, 122707. [CrossRef]
21. Zeng, J.; Li, Y.; Hou, Y.; Gao, C.; Yuan, J. Ionization potential depression and ionization balance in dense carbon plasma under solar and stellar interior conditions. *Astron. Astrophys.* **2020**, *644*, A92. [CrossRef]
22. Pain, J.C. Multi-Configuration Calculation of Ionization Potential Depression. *Plasma* **2022**, *5*, 384–407. [CrossRef]
23. Pain, J.C.; Dejonghe, G.; Blenski, T. Quantum-mechanical model for the study of pressure ionization in the super configuration approach. *J. Phys. A Math. Gen.* **2006**, *39*, 4659–4666. [CrossRef]
24. Pain, J.C.; Dejonghe, G.; Blenski, T. A self-consistent model for the study of electronic properties of hot dense plasmas. *J. Quant. Spectrosc. Radiat. Transf.* **2006**, *99*, 451–468. [CrossRef]
25. Zeng, J.; Li, Y.; Gao, C.; Yuan, J. Screening potential and continuum lowering in a dense plasma under solar-interior conditions. *Astron. Astrophys.* **2020**, *634*, A117. [CrossRef]

26. Zeng, J.; Ye, C.; Li, Y.; Yuan, J. Ionization potential depression in dense iron plasmas near solid density. *Results Phys.* **2022**, *40*, 105836. [CrossRef]
27. Preston, T.R.; Vinko, S.M.; Ciricosta, O.; Chung, H.K.; Lee, R.W.; Wark, J.S. The effects of ionization potential depression on the spectra emitted by hot dense aluminium plasmas. *High Energy Density Phys.* **2013**, *9*, 258–263. [CrossRef]
28. Son, S.K.; Thiele, R.; Jurek, Z.; Ziaja, B.; Santra, R. Quantum-mechanical calculation of ionization-potential lowering in dense plasmas. *Phys. Rev. X* **2014**, *4*, 031004. [CrossRef]
29. Iglesias, C.A. A plea for a reexamination of ionization potential depression measurements. *High Energy Density Phys.* **2014**, *12*, 5–11. [CrossRef]
30. Hansen, S.B.; Colgan, J.; Faenov, A.Y.; Abdallah, J.; Pikuz, S.A.; Skobelev, I.Y.; Wagenaars, E.; Booth, N.; Culfa, O.; Dance, R.J.; et al. Detailed analysis of hollow ions spectra from dense matter pumped by X-ray emission of relativistic laser plasma. *Phys. Plasmas* **2014**, *21*, 031213. [CrossRef]
31. Crowley, B.J.B. Continuum lowering–A new perspective. *High Energy Density Phys.* **2014**, *13*, 84–102. [CrossRef]
32. Calisti, A.; Ferri, S.; Talin, B. Ionization potential depression for non equilibrated aluminum plasmas. *J. Phys. B At. Mol. Opt. Phys.* **2015**, *48*, 224003. [CrossRef]
33. Vinko, S.M.; Ciricosta, O.; Wark, J.S. Density functional theory calculations of continuum lowering in strongly coupled plasmas. *Nat. Commun.* **2014**, *5*, 3533. [CrossRef]
34. Hu, S.X. Continuum lowering and fermi-surface rising in strongly coupled and degenerate plasmas. *Phys. Rev. Lett.* **2017**, *119*, 065001. [CrossRef] [PubMed]
35. Stransky, M. Monte Carlo simulations of ionization potential depression in dense plasmas. *Phys. Plasmas* **2016**, *23*, 012708. [CrossRef]
36. Lin, C.; Röpke, G.; Kraeft, W.D.; Reinholz, H. Ionization-potential depression and dynamical structure factor in dense plasmas. *Phys. Rev. E* **2017**, *96*, 013202. [CrossRef] [PubMed]
37. Kasim, M.F.; Wark, J.S.; Vinko, S.M. Validating continuum lowering models via multi-wavelength measurements of integrated X-ray emission. *Sci. Rep.* **2018**, *8*, 6276. [CrossRef]
38. Ali, A.; Naz, G.S.; Shahzad, M.S.; Kouser, R.; Nasim, M.H. Improved continuum lowering calculations in screened hydrogenic model with l-splitting for high energy density systems. *High Energy Density Phys.* **2018**, *26*, 48–55. [CrossRef]
39. Röpke, G.; Blaschke, D.; Döppner, T.; Lin, C.; Kraeft, W.D.; Redmer, R.; Reinholz, H. Ionization potential depression and Pauli blocking in degenerate plasmas at extreme densities. *Phys. Rev. E* **2019**, *99*, 033201. [CrossRef]
40. Kraus, D.; Bachmann, B.; Barbrel, B.; Falcone, R.W.; Fletcher, L.B.; Frydrych, S.; Gamboa, E.J.; Gauthier, M.; Gericke, D.O.; Glenzer, S.H.; et al. Characterizing the ionization potential depression in dense carbon plasmas with high-precision spectrally resolved X-ray scattering. *Plasma Phys. Control. Fusion* **2018**, *61*, 014015. [CrossRef]
41. Ciricosta, O.; Vinko, S.M.; Barbrel, B.; Rackstraw, D.S.; Preston, T.R.; Burian, T.; Chalupský, J.; Cho, B.I.; Chung, H.-K.; Dakovski, G.L.; et al. Measurements of continuum lowering in solid-density plasmas created from elements and compounds. *Nat. Commun.* **2016**, *7*, 11713. [CrossRef]
42. Hoarty, D.J.; Allan, P.; James, S.F.; Brown, C.R.D.; Hobbs, L.M.R.; Hill, M.P.; Harris, J.W.O.; Morton, J.; Brookes, M.G.; Shepherd, R.; et al. Observations of the Effect of Ionization-Potential Depression in Hot Dense Plasma. *Phys. Rev. Lett.* **2013**, *110*, 265003. [CrossRef]
43. LCLS. Available online: http://lcls.slac.stanford.edu/ (accessed on 14 September 2023).
44. Fletcher, L.B.; Kritcher, A.L.; Pak, A.; Ma, T.; Döppner, T.; Fortmann, C.; Divol, L.; Jones, O.S.; Landen, O.L.; Scott, H.A.; et al. Observations of Continuum Depression in Warm Dense Matter with X-ray Thomson Scattering. *Phys. Rev. Lett.* **2014**, *112*, 145004. [CrossRef]
45. Kraus, D.; Chapman, D.A.; Kritcher, A.L.; Baggott, R.A.; Bachmann, B.; Collins, G.W.; Glenzer, S.H.; Hawreliak, J.A.; Kalantar, D.H.; Landen, O.L.; et al. X-ray scattering measurements on imploding CH spheres at the National Ignition Facility. *Phys. Rev. E* **2016**, *94*, 011202. [CrossRef]
46. Bowen, L.; Chenzhong, D.; Jun, J.; Jianguo, W. Atomic Structures and Radiative Properties of He-like Ions in Debye Plasmas. *Plasma Sci. Technol.* **2010**, *12*, 373. [CrossRef]
47. Okutsu, H.; Sako, T.; Yamanouchi, K.; Diercksen, G.H. Electronic structure of atoms in laser plasmas: A Debye shielding approach. *J. Phys. B At. Mol. Opt. Phys.* **2005**, *38*, 917. [CrossRef]
48. Saha, J.K.; Bhattacharyya, S.; Mukherjee, T.K.; Mukherjee, P.K. 2pnp (1, 3Pe) states of neutral He and Li+ ions under Debye plasma screening. *J. Phys. B At. Mol. Opt. Phys.* **2009**, *42*, 245701. [CrossRef]
49. Saha, J.K.; Mukherjee, T.K.; Mukherjee, P.K.; Fricke, B. Effect of strongly coupled plasma on the doubly excited states of helium like ions. *Eur. Phys. J. D* **2012**, *66*, 43-1–43-9. [CrossRef]
50. Sil, A.N.; Mukherjee, P.K. Effect of debye plasma on the doubly excited states of highly stripped ions. *Int. J. Quant. Chem.* **2005**, *102*, 1061–1068. [CrossRef]
51. Belkhiri, M.; Fontes, C.J.; Poirier, M. Influence of the plasma environment on atomic structure using an ion-sphere model. *Phys. Rev. A* **2015**, *92*, 032501. [CrossRef]
52. Chen, Z.B. Spectroscopy characteristics and decay properties of plasma-embedded atoms in external electric and magnetic fields. *Phys. Plasmas* **2022**, *29*, 062108. [CrossRef]

53. Jin, R.; Jurek, Z.; Santra, R.; Son, S.K. Plasma environmental effects in the atomic structure for simulating X-ray free-electron-laser-heated solid-density matter. *Phys. Rev. E* **2022**, *106*, 015206. [CrossRef] [PubMed]
54. Li, X.; Xu, Z.; Rosmej, F.B. Exchange energy shifts under dense plasma conditions. *J. Phys. B At. Mol. Opt. Phys.* **2006**, *39*, 3373. [CrossRef]
55. Singh, A.K.; Dawra, D.; Dimri, M.; Jha, A.K.S.; Pandey, R.K.; Mohan, M. Plasma screening effects on the atomic structure of He-like ions embedded in strongly coupled plasma. *Phys. Lett. A* **2020**, *384*, 126369. [CrossRef]
56. Saha, B.; Fritzsche, S. Influence of dense plasma on the low-lying transitions in Be-like ions: Relativistic multiconfiguration Dirac–Fock calculation. *J. Phys. B At. Mol. Opt. Phys.* **2007**, *40*, 259. [CrossRef]
57. Li, Y.; Wu, J.; Hou, Y.; Yuan, J. Influence of hot and dense plasmas on energy levels and oscillator strengths of ions: Beryllium-like ions for Z = 26–36. *J. Phys. B At. Mol. Opt. Phys.* **2008**, *41*, 145002. [CrossRef]
58. Dimri, M.; Dawra, D.; Singh, A.K.; Pandey, R.K.; Kumar, P.; Jha, A.K.S.; Mohan, M. Influence of strongly coupled plasma on the low-lying transitions of Be-like ions. *Eur. Phys. J. D* **2022**, *76*, 223. [CrossRef]
59. Beiersdorfer, P.; Brown, G.V.; McKelvey, A.; Shepherd, R.; Hoarty, D.J.; Brown, C.R.D.; Hill, M.P.; Hobbs, L.M.R.; James, S.F.; Morton, J.; et al. High-resolution measurements of Cl^{15+} line shifts in hot, solid-density plasmas. *Phys. Rev. A* **2019**, *100*, 012511. [CrossRef]
60. Hansen, S.B.; Harding, E.C.; Knapp, P.F.; Gomez, M.R.; Nagayama, T.; Bailey, J.E. Changes in the electronic structure of highly compressed iron revealed by X-ray fluorescence lines and absorption edges. *High Energy Density Phys.* **2017**, *24*, 39–43. [CrossRef]
61. Stillman, C.R.; Nilson, P.M.; Ivancic, S.T.; Golovkin, I.E.; Mileham, C.; Begishev, I.A.; Froula, D.H. Picosecond time-resolved measurements of dense plasma line shifts. *Phys. Rev. E* **2017**, *95*, 063204. [CrossRef] [PubMed]
62. Khattak, F.Y.; du Sert, O.P.; Rosmej, F.B.; Riley, D. Evidence of plasma polarization shift of Ti He-α resonance line in high density laser produced plasmas. *J. Phys. Conf. Ser.* **2012**, *397*, 012020. [CrossRef]
63. Vinko, S.M.; Ciricosta, O.; Cho, B.I.; Engelhorn, K.; Chung, H.K.; Brown, C.R.D.; Burian, T.; Chalupský, J.; Falcone, R.W.; Graves, C.; et al. Creation and diagnosis of a solid-density plasma with an X-ray free-electron laser. *Nature* **2012**, *482*, 59–62. [CrossRef]
64. Ciricosta, O.; Vinko, S.M.; Chung, H.K.; Cho, B.I.; Brown, C.R.D.; Burian, T.; Chalupský, J.; Engelhorn, K.; Falcone, R.W.; Graves, C.; et al. Direct measurements of the ionization potential depression in a dense plasma. *Phys. Rev. Lett.* **2012**, *109*, 065002. [CrossRef]
65. Saemann, A.; Eidmann, K.; Golovkin, I.E.; Mancini, R.C.; Andersson, E.; Förster, E.; Witte, K. Isochoric heating of solid aluminum by ultrashort laser pulses focused on a tamped target. *Phys. Rev. Lett.* **1999**, *82*, 4843. [CrossRef]
66. Emma, P.; Akre, R.; Arthur, J.; Bionta, R.; Bostedt, C.; Bozek, J.; Brachmann, A.; Bucksbaum, P.; Coffee, R.; Decker, F.J.; et al. First lasing and operation of an ångstrom-wavelength free-electron laser. *Nat. Photonics* **2010**, *4*, 641–647. [CrossRef]
67. Rosmej, F.B.; Lee, R.W. Hollow ion emission driven by pulsed intense X-ray fields. *Europhys. Lett.* **2007**, *77*, 24001. [CrossRef]
68. Galtier, E.; Rosmej, F.B.; Dzelzainis, T.; Riley, D.; Khattak, F.Y.; Heimann, P.; Lee, R.W.; Nelson, A.J.; Vinko, S.M.; Whitcher, T.; et al. Decay of cystalline order and equilibration during the solid-to-plasma transition induced by 20-fs microfocused 92-eV free-electron-laser pulses. *Phys. Rev. Lett.* **2011**, *106*, 164801. [CrossRef] [PubMed]
69. Falcon, R.E.; Rochau, G.A.; Bailey, J.E.; Gomez, T.A.; Montgomery, M.H.; Winget, D.E.; Nagayama, T. Laboratory measurements of white dwarf photospheric spectral lines: Hβ. *Astrophys. J.* **2015**, *806*, 214. [CrossRef]
70. Fontes, C.J.; Fryer, C.L.; Hungerford, A.L.; Hakel, P.; Colgan, J.; Kilcrease, D.P.; Sherrill, M.E. Relativistic opacities for astrophysical applications. *High Energy Density Phys.* **2015**, *16*, 53–59. [CrossRef]
71. Schaeuble, M.A.; Nagayama, T.; Bailey, J.E.; Gomez, T.A.; Montgomery, M.H.; Winget, D.E. Hβ and Hγ absorption-line profile inconsistencies in laboratory experiments performed at white dwarf photosphere conditions. *Astrophys. J.* **2019**, *885*, 86. [CrossRef]
72. Hansen, S.B. Investigating inertial confinement fusion target fuel conditions through X-ray spectroscopy. *Phys. Plasmas* **2012**, *19*, 056312. [CrossRef]
73. Deschaud, B.; Peyrusse, O.; Rosmej, F.B. Simulation of XFEL induced fluorescence spectra of hollow ions and studies of dense plasma effects. *Phys. Plasmas* **2020**, *27*, 063303. [CrossRef]
74. Woltz, L.A.; Hooper, C.F., Jr. Full Coulomb calculation of Stark broadening in laser-produced plasmas. *Phys. Rev. A* **1984**, *30*, 468. [CrossRef]
75. Jung, Y.D. Orientation phenomena for the 1 s $\to$ 2p $\pm$ 1 atomic collisional excitations in quantum plasmas: Shielding and plasmon coupling. *Phys. Plasmas* **2012**, *19*, 113301. [CrossRef]
76. Kim, C.G.; Jung, Y.D. Quantum screening effects on dipole and quadrupole electron-impact excitation channels in dense high-temperature plasmas. *Phys. Plasmas* **2002**, *9*, 4040–4044. [CrossRef]
77. Kim, C.G.; Jung, Y.D. Quantum dynamic screening effects on the elastic collisions in strongly coupled semiclassical plasmas. *Phys. Plasmas* **2012**, *19*, 014502. [CrossRef]
78. Liu, L.; Wang, J.G.; Janev, R.K. Dynamics of He^{2+} + H (1 s) excitation and electron-capture processes in Debye plasmas. *Phys. Rev. A* **2008**, *77*, 032709. [CrossRef]
79. Stewart, J.C.; Pyatt, K.D., Jr. Lowering of ionization potentials in plasmas. *Astrophys. J.* **1966**, *144*, 1203. [CrossRef]
80. Rosmej, F.; Bennadji, K.; Lisitsa, V.S. Effect of dense plasmas on exchange-energy shifts in highly charged ions: An alternative approach for arbitrary perturbation potentials. *Phys. Rev. A* **2011**, *84*, 032512. [CrossRef]
81. Rosmej, F.B. Ionization potential depression in an atomic-solid-plasma picture. *J. Phys. B At. Mol. Phys.* **2018**, *51*, 09LT01. [CrossRef]

82. Piron, R.; Blenski, T. Variational-average-atom-in-quantum-plasmas (VAAQP) code and virial theorem: Equation-of-state and shock-Hugoniot calculations for warm dense Al, Fe, Cu, and Pb. *Phys. Rev. E* **2011**, *83*, 026403. [CrossRef] [PubMed]
83. Chen, Z.B. Theoretical evaluation of excitation cross section and fluorescence polarization of a solid-density Si plasma. *Phys. Plasmas* **2022**, *29*, 022106. [CrossRef]
84. Pradhan, A. Photoionization and Opacity. *Atoms* **2023**, *11*, 52. [CrossRef]
85. Qi, Y.Y.; Wang, J.G.; Janev, R.K. Photoionization of hydrogen-like ions in dense quantum plasmas. *Phys. Plasmas* **2017**, *24*, 062110. [CrossRef]
86. Chen, Z.B.; Wang, K. Photoionization of H-like C^{5+} ion in the presence of a strongly coupled plasma environment. *J. Quant. Spectrosc. Radiat. Transfer* **2020**, *245*, 106847. [CrossRef]
87. Lin, C.Y.; Ho, Y.K. Quadrupole photoionization of hydrogen atoms in Debye plasmas. *Phys. Plasmas* **2010**, *17*, 093302. [CrossRef]
88. Rosmej, F.B.; Vainshtein, L.A.; Astapenko, V.A.; Lisitsa, V.S. Statistical and quantum photoionization cross sections in plasmas: Analytical approaches for any configurations including inner shells. *Matter Radiat. Extrem.* **2020**, *5*, 064202. [CrossRef]
89. Ma, K.; Chen, C.; Chu, Y.; Jiao, Z.; Chen, Z.B. Theoretical Calculations on the Relativistic Corrections and Photoionization Cross Sections for Hydrogen like Ions in Finite Temperature Dense Plasmas. *Few-Body Syst.* **2022**, *63*, 69. [CrossRef]
90. Dawra, D.; Dimri, M.; Singh, A.K.; Jha, A.K.S.; Pandey, R.K.; Sharma, R.; Mohan, M. Influence of strongly coupled plasma environment on photoionization of H-like O^{7+} ion. *Phys. Plasmas* **2021**, *28*, 112706. [CrossRef]
91. Li, X.; Rosmej, F.B. Analytical approach to level delocalization and line shifts in finite temperature dense plasmas. *Phys. Lett. A* **2020**, *384*, 126478. [CrossRef]
92. Deb, N.C.; Sil, N.C. Electron impact excitation of positive ions in dense plasma. *J. Phys. B At. Mol. Phys.* **1984**, *17*, 3587. [CrossRef]
93. Whitten, B.L.; Lane, N.F.; Weisheit, J.C. Plasma-screening effects on electron-impact excitation of hydrogenic ions in dense plasmas. *Phys. Rev. A* **1984**, *29*, 945. [CrossRef]
94. Jung, Y.D.; Yoon, J.S. Electron-Impact Excitations of Hydrogenic Ions in Strongly Coupled Plasmas. *Astrophys. J.* **2000**, *530*, 1085. [CrossRef]
95. Chen, Z.B.; Qi, Y.Y.; Sun, H.Y.; Zhao, G.P.; Liu, P.F. Density and temperature dependence of the cross sections after excitation of Ar XVIII by electron impact. *Phys. Plasmas* **2021**, *28*, 052109. [CrossRef]
96. Singh, J.; Dawra, D.; Verma, N.; Jha, A.K.S.; Kumar, P.; Dimri, M.; Mohan, M. Study of electron impact excitation of H-like Si^{13+} ion in dense plasma environment. *New Astron.* **2023**, *101*, 102001. [CrossRef]
97. Kornev, A.S.; Chernov, V.E.; Kubelík, P.; Ferus, M. Modification of Vibrational Parameters of a D∞h-Symmetric Triatomic Molecule in a Laser Plasma. *Symmetry* **2022**, *14*, 2382. [CrossRef]
98. Kuzenov, V.V.; Ryzhkov, S.V.; Shumaev, V.V. Numerical thermodynamic analysis of alloys for plasma electronics and advanced technologies. *Probl. At. Sci. Technol.* **2015**, *4*, 53–56.
99. Bergmann, K. Extreme Ultraviolet Radiation Sources from Dense Plasmas. *Atoms* **2023**, *11*, 118. [CrossRef]
100. Glazov, D.A.; Zinenko, D.V.; Agababaev, V.A.; Moshkin, A.D.; Tryapitsyna, E.V.; Volchkova, A.M.; Volotka, A.V. g Factor of Few-Electron Highly Charged Ions. *Atoms* **2023**, *11*, 119. [CrossRef]
101. Murillo, M.S.; Weisheit, J.C. Dense plasmas, screened interactions, and atomic ionization. *Phys. Rep.* **1998**, *302*, 1–65. [CrossRef]
102. Janev, R.K.; Zhang, S.; Wang, J.; Liu, L.; Wang, J.G.; Meng, G.; Wang, X.; Li, J.; Zhang, W.; He, B.; et al. Review of quantum collision dynamics in Debye plasmas. *Matter Radiat. Extrem.* **2016**, *1*, 237. [CrossRef]
103. Rouse, C.A. Finite electronic partition function from screened Coulomb interactions. *Phys. Rev.* **1967**, *163*, 62. [CrossRef]
104. Margenau, H.; Lewis, M. Structure of spectral lines from plasmas. *Rev. Mod. Phys.* **1959**, *31*, 569. [CrossRef]
105. Chang, T.N.; Fang, T.K. Atomic photoionization in a changing plasma environment. *Phys. Rev. A* **2013**, *88*, 023406. [CrossRef]
106. Rouse, C.A. Screened Coulomb solutions of the Schrödinger equation. *Phys. Rev.* **1967**, *159*, 41. [CrossRef]
107. Ecker, G.; Kröll, W. Lowering of the ionization energy for a plasma in thermodynamic equilibrium. *Phys. Fluids* **1963**, *6*, 62–69. [CrossRef]
108. Ecker, G.; Weizel, W. Zustandssumme und effektive Ionisierungsspannung eines Atoms im Inneren des Plasmas. *Ann. Phys.* **1956**, *452*, 126–140. [CrossRef]
109. Chen, Z.B.; Ma, K.; Hu, H.W.; Wang, K. Relativistic effects on the energy levels and radiative properties of He-like ions immersed in Debye plasmas. *Phys. Plasmas* **2018**, *25*, 072120. [CrossRef]
110. Clayton, D.D. *Principles of Stellar Evolution and Nucleosynthesis*; University of Chicago Press: Chicago, IL, USA, 1983.
111. Weisheit, J.C. Atomic excitation in dense plasmas. *Adv. At. Mol. Phys.* **1989**, *25*, 101.
112. Scheibner, K.; Weisheit, J.C.; Lane, N.F. Plasma screening effects on proton-impact excitation of positive ions. *Phys. Rev. A* **1987**, *35*, 1252. [CrossRef] [PubMed]
113. Chen, Z.B.; Hu, H.W.; Ma, K.; Liu, X.B.; Guo, X.L.; Li, S.; Zhu, B.H.; Huang, L.; Wang, K. Influence of dense plasma on the energy levels and transition properties in highly charged ions. *Phys. Plasmas* **2018**, *25*, 032108. [CrossRef]
114. Li, X.; Rosmej, F.B.; Lisitsa, V.S.; Astapenko, V.A. An analytical plasma screening potential based on the self-consistent-field ion-sphere model. *Phys. Plasmas* **2019**, *26*, 033301. [CrossRef]
115. Li, X.; Rosmej, F.B. Spin-dependent energy-level crossings in highly charged ions due to dense plasma environments. *Phys. Rev. A* **2010**, *82*, 022503. [CrossRef]
116. Available online: http://amdpp.phys.strath.ac.uk/rmatrix/ser/darc/ (accessed on 10 September 2023).
117. Gu, M.F. The flexible atomic code. *Can. J. Phys.* **2008**, *86*, 675–689. [CrossRef]

118. Dawra, D.; Dimri, M.; Singh, A.K.; Jha, A.K.S.; Singh, S.S. Effect of Dense Plasma Environment on the Spectroscopic Properties of He-like Ca^{18+} Ion. *J. At. Mol. Condens. Nano Phys.* **2019**, *6*, 103. [CrossRef]
119. Singh, A.K.; Dawra, D.; Dimri, M.; Jha, A.K.S.; Mohan, M. Relativistic atomic structure calculations and study of plasma parameters for Na-like Se XXIV. *Phys. Plasmas* **2019**, *26*, 062704. [CrossRef]
120. Singh, A.K.; Dimri, M.; Dawra, D.; Jha, A.K.S.; Mohan, M. Accurate study on the properties of spectral lines for Na-like Cr^{13+}. *Can. J. Phys.* **2019**, *97*, 436–442. [CrossRef]
121. Dimri, M.; Dawra, D.; Singh, A.K.; Jha, A.K.S.; Pandey, R.K.; Sharma, R.; Mohan, M. Fine structure calculations of excitation energies, lifetimes and radiative properties of S-like Kr XXI. *Radiat. Phys. Chem.* **2021**, *189*, 109756. [CrossRef]
122. Dimri, M.; Dawra, D.; Singh, A.K.; Jha, A.K.S.; Pandey, R.K.; Mohan, M. Atomic structure and radiative properties of He-like Ni26+ ion in dense plasma. *Can. J. Phys.* **2021**, *99*, 559–565. [CrossRef]
123. Dawra, D.; Dimri, M.; Singh, A.K.; Pandey, R.K.; Jha, A.K.S.; Mohan, M. Influence of Dense Plasma Environment on the He-α and He-β Transitions of Cl15+ Ion. In *Proceedings of the International Conference on Atomic, Molecular, Optical & Nano Physics with Applications*; Springer: Singapore, 2022.
124. Singh, A.K.; Dimri, M.; Dawra, D.; Jha, A.K.S.; Verma, N.; Mohan, M. Spectroscopic study of EUV and SXR transitions of Cu XIX with plasma parameters. *Radiat. Phys. Chem.* **2019**, *156*, 174–192. [CrossRef]
125. Kramida, A.; Ralchenko, Y.; Reader, J.; NIST ASD Team. National Institute of Standards and Technology, Gaithersburg, MD, 2023. Available online: https://physics.nist.gov/PhysRefData/ASD/levels_form.html (accessed on 10 September 2023).
126. Kogan, V.I.; Kukushkin, A.B.; Lisitsa, V.S. Kramers electrodynamics and electron-atomic radiative-collisional processes. *Phys. Rep.* **1992**, *213*, 1–116. [CrossRef]